ALEXANDRE DAZZI
LABORATORIE DE CHIMIE PHYSIQUE, UNIVERSITÉ PARIS-SUD, 91405 ORSAY, FRANCE

CRAIG B. PRATER AND QICHI HU
ANASYS INSTRUMENTS, 121 GRAY AVENUE, SUITE 100, SANTA BARBARA, CA 93101 USA

D. BRUCE CHASE AND JOHN F. RABOLT
DEPARTMENT OF MATERIALS SCIENCE AND ENGINEERING, THE UNIVERSITY OF DELAWARE, NEWARK, DE 19716 USA

CURTIS MARCOTT
LIGHT LIGHT SOLUTIONS, LLC, P.O. BOX 81486, ATHENS, GA 30608 USA

AFM–IR: Combining Atomic Force Microscopy and Infrared Spectroscopy for Nanoscale Chemical Characterization

Polymer and life science applications of a technique that combines atomic force microscopy (AFM) and infrared (IR) spectroscopy to obtain nanoscale IR spectra and images are reviewed. The AFM–IR spectra generated from this technique contain the same information with respect to molecular structure as conventional IR spectroscopy measurements, allowing significant leverage of existing expertise in IR spectroscopy. The AFM–IR technique can be used to acquire IR absorption spectra and absorption images with spatial resolution on the 50 to 100 nm scale, versus the scale of many micrometers or more for conventional IR spectroscopy. In the life sciences, experiments have demonstrated the capacity to perform chemical spectroscopy at the sub-cellular level. Specifically, the AFM–IR technique provides a label-free method for mapping IR-absorbing species in biological materials. On the polymer side, AFM–IR was used to map the IR absorption properties of polymer blends, multilayer films, thin films for active devices such as organic photovoltaics, microdomains in a semicrystalline polyhydroxyalkanoate copolymer, as well as model pharmaceutical blend systems. The ability to obtain spatially resolved IR spectra as well as high-resolution chemical images collected at specific IR wavenumbers was demonstrated. Complementary measurements mapping variations in sample stiffness were also obtained by tracking changes in the cantilever contact resonance frequency. Finally, it was shown that by taking advantage of the ability to arbitrarily control the polarization direction of the IR excitation laser, it is possible to obtain important information regarding molecular orientation in electrospun nanofibers.

Index Headings: **Infrared microspectroscopy; Atomic force microscopy; AFM; IR; Near field; *E. coli*; Polymer; Poly(hydroxybutyrate); PHB; Organic photovoltaics; P3HT; PCMB; Poly(-hydroxyalkanoate); PHA; Phase separation; Miscibility; Pharmaceutical formulation; Nanofibers; Molecular orientation; Poly(vinylidene fluoride); PVDF.**

INTRODUCTION

Infrared (IR) spectroscopy in the 2.5 to 20 μm (500–4000 cm^{-1}) range (mid-IR) is a direct probe of the molecular vibrations in a sample. IR absorption spectra of organic compounds are often used to specifically identify chemical species. By combining microscopy and spectroscopy, chemical analysis can be done on a micrometer scale. Over the last several years, technology upgrades in optics (e.g., aberration correction and improvement of confocal microscopy) and in detection (e.g., better sensitivity of IR detectors and focal plane arrays) have improved the performance of microspectroscopy.[1–5] As such, IR microspectroscopy has become an attractive tool for polymer and life sciences.

One of the main limitations of conventional IR microspectroscopy, however, is spatial resolution. The optical diffraction limit along with other practical limitations has limited spatial resolution to the range of 3–30 μm, depending on the wavelength of light and instrumentation used. There is a compelling need to improve the lateral resolution beyond the diffraction limit in order to apply the power of IR spectroscopy at finer length scales for a wide range of materials. Several near-field approaches have been developed during the past 20 years to overcome this limitation. In many of these approaches, the sharp tip of a scanning probe microscope is used to sample and/or enhance the radiation interacting within a nanoscale region of a sample. Research advances in near-field optics have been numerous and exciting in the visible range, and in recent years were extended into the IR.[6–17] Although there is some very good work in IR, there are still significant challenges. The main issues are associated with the lack of broadly tunable IR sources and challenges associated with obtaining interpretable spectra. The spectrum that is measured in the near-field regime depends not only on sample absorption, but also on complex tip-sample scattering phenomena.[18] The observed spectral bands can be shifted with respect to expected absorption bands, and the shift depends on the sample, tip geometries, and tip position.

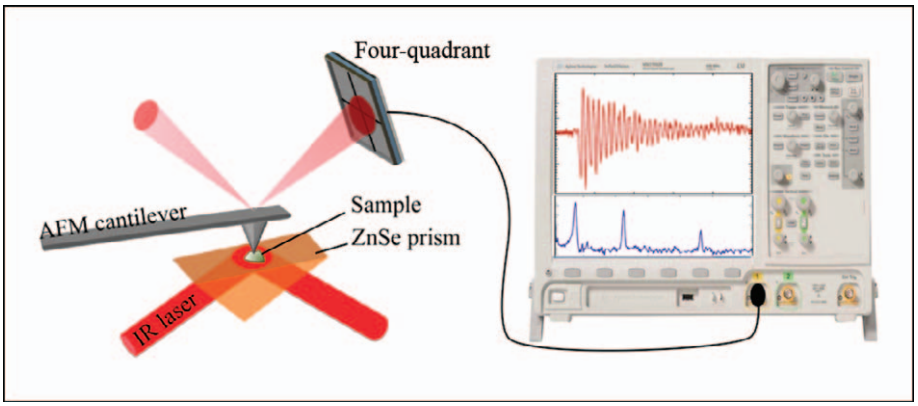

FIG. 1. Scheme of the AFM–IR setup. The AFM cantilever ring-down amplitude plotted as a function of laser excitation wavelength produces the IR spectrum.

Therefore it is highly desirable to have a technique that can provide interpretable IR absorption spectra that are comparable to conventional IR spectroscopy techniques such as Fourier transform IR (FT–IR) spectroscopy. After several years of work in near-field IR optics with these different techniques, we developed, with our coworkers, another method based on photothermal-induced absorption. The technique, called atomic force microscopy (AFM)–IR,[19] irradiates a region of a sample with light from a tunable IR laser and measures the resulting photothermal expansion of the sample with the tip of an atomic force microscope. The first experimental setup was established in the Centre Laser Infrarouge d'Orsay (CLIO) in the Laboratoire de Chimie Physique by using a free-electron laser as the tunable IR source. The AFM–IR instrument at CLIO has been used for the last five years, resulting in publications in different domains such as nanophotonics,[20–22] cellular biology,[23] and microbiology.[24–26] The AFM–IR instrument remains available for external scientific collaborations as a user facility at CLIO. In 2010, the American company Anasys Instruments, Inc., commercialized a version of AFM–IR[27,28] by using a bench-top tunable IR laser, based on an optical parametric oscillator.

BASIC PRINCIPLES OF AFM–IR

In AFM–IR, the sample is placed on an IR transparent prism (e.g., ZnSe) and irradiated with a total internal reflection style illumination scheme, as shown in Fig. 1. If the IR laser is tuned to a wavelength corresponding to absorption by the sample, the absorbed light induces a photothermal response in the sample. That is, the absorbed light is converted into heat, which results in rapid thermal expansion of the absorbing region of the sample.[19] The rapid thermal expansion pulse is then detected with the tip of an atomic force microscope. The thermal expansion signal detected by the AFM tip is directly proportional to the absorption coefficient of the sample (a complete derivation of this is given in the Appendix.) In brief, thermal expansion of the sample occurs only when molecular vibrations excited by absorbed IR photons from the tunable laser source return to their ground vibrational state though the transfer of energy in the form of heat to the lattice. Thus, the detection scheme is analogous to photoacoustic spectroscopy, except that the AFM tip and cantilever are used to detect and amplify the thermal expansion signal instead of a microphone in a gas cell. Because the signal detected in AFM–IR is in proportion to the sample absorption, absorption spectra obtained by the AFM–IR technique correlate very well to conventional IR absorption spectra collected in transmission. Using an AFM tip to detect the thermal expansion pulse is the key to measuring IR absorption below the conventional diffraction limit. The AFM tip can sense and map variations in thermal expansion from IR absorption

to better than 100 nm spatial resolution. Further, the AFM detection sensitivity is sufficient to enable chemical identification of samples at a scale of tens of nanometers.

AFM–IR Setup Description. A schematic of the AFM–IR system is shown in Fig. 1. The tunable IR laser light enters the IR transparent 45° ZnSe prism (internal reflectance element) at normal incidence. The laser light is entirely internally reflected at the interface between the prism and the sample for most organic materials, with a refractive index around 1.5. A standing wave, or evanescent field, is produced, which extends through the sample film to a distance on the order of the wavelength of light. Importantly, the total internal reflection conditions of the experimental setup reduce any background interaction of the tunable laser light directly with the AFM cantilever.

The tip of the AFM is in contact with the sample under study. With each laser pulse, the sample's thermal expansion induces a brief force impulse on the tip, inducing ringing at the AFM cantilever's resonant frequencies. The oscillation signal of the cantilever is recorded by reflecting a visible laser off the top surface of the cantilever and measuring its position with the four-quadrant detector of the AFM. The signal can be simultaneously analyzed via fast Fourier transform (FFT) to determine the amplitudes and frequencies of the cantilever vibrational modes.[29,30] The raw cantilever ring-down signal usually contains multiple resonant frequency components. Measuring the amplitudes of the cantilever oscillation as a function of the source wavelength creates local absorption spectra. Typically, the height of the most intense cantilever ring-down peak in the FFT spectrum of the raw cantilever ring-down signal is measured for each wavelength as the laser source is stepped one wavelength at a time through the spectral region of interest. The IR spectrum is then obtained by plotting the laser wavenumber on the *x* axis versus the cantilever ring-down amplitude on the *y* axis.

Experimental Demonstration. *Escherichia coli* is a good test sample because of the average size of this bacterium (2 to 6 μm long, 1 μm wide, 500 nm high), and the absorption bands are known and assigned, for example, amide I at 1650 cm^{-1}, amide II at 1550 cm^{-1}, and DNA (phosphate backbone) at 1080 cm^{-1}. To prepare the surface of the prism, a large amount of bacteria were centrifuged and washed with distilled water to eliminate their nutritive environment. A suspension of bacteria was then deposited on the prism surface and heated at 30 °C to slowly evaporate the water. The final concentration of bacteria on the surface was typically 10 to 20 bacteria over 100 × 100 μm. By using this method, we obtained intact bacteria that kept their original shape. The absorption bands in the mid-IR were still present even when the bacteria were dried. After an AFM scan on the prism surface, we could select a single bacterium and make different analyses as a function of tip position and laser wavelength.

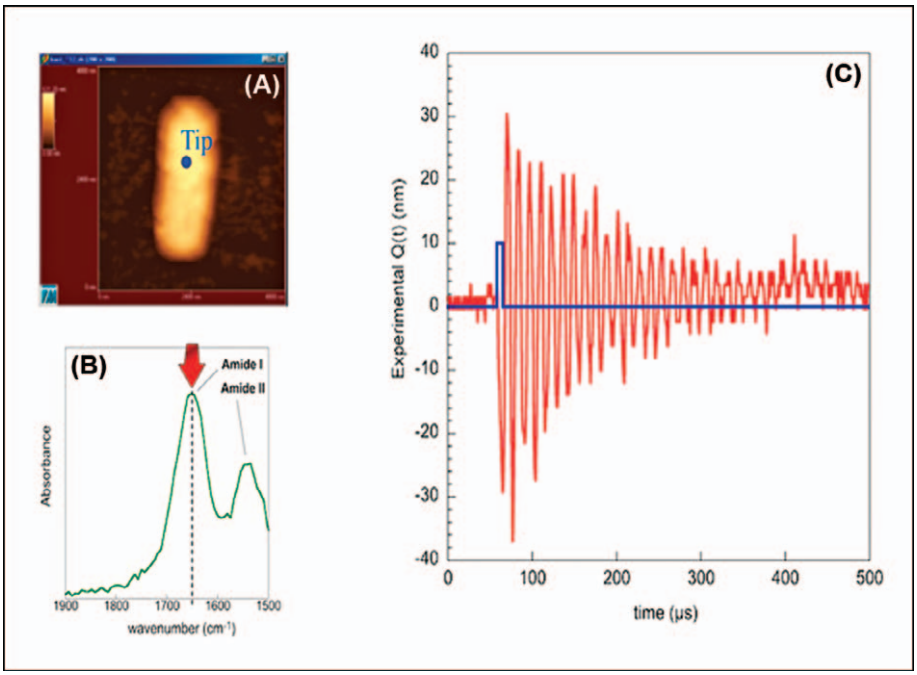

Fig. 2. **(a)** ***AFM topography picture of the bacterium; the position of the tip is indicated in blue.*** **(b)** ***FT–IR spectrum; the bacterium absorption spectrum is drawn in green, and the wavenumber of the CLIO laser is indicated by the red arrow.*** **(c)** ***Oscillations recorded by the four-quadrant detector (in red) as function of time superposed on the CLIO pulse laser (blue).***

Figure 2 shows some AMF-IR measurements on an *E. coli* cell. First, the AFM tip was positioned on the bacterium with a static force of around 10 nN. The laser wavelength was centered on the amide I band at 1650 cm^{-1}, corresponding to a strong absorption in protein. After each laser pulse, we observed decaying oscillations with initial amplitude of ~30 nm, which decreased with a time constant of close to 200 μs. The amplitude of oscillations (~30 nm) was always smaller than the static deflection (~300 nm at 10 nN of applied force), ensuring that the tip stayed in contact with the bacterium.

One potential concern was the possibility that the cantilever could respond directly to IR light striking the cantilever, rather than by absorption of IR light by the sample. Such an effect was observed by Hill et al. when using an axial illumination system.[31] To test this possibility, the cantilever deflection was recorded outside the bacterium, keeping the laser wavenumber at the same value of 1650 cm^{-1}. In this case (Fig. 3), we did not observe the background absorption seen by Hill; the measured cantilever deflection signal off of the bacterium showed only noise. This proves that cantilever oscillations are only excited by the bacterium expansion and not by absorption and heating of the cantilever. This illustrates an advantage of the total

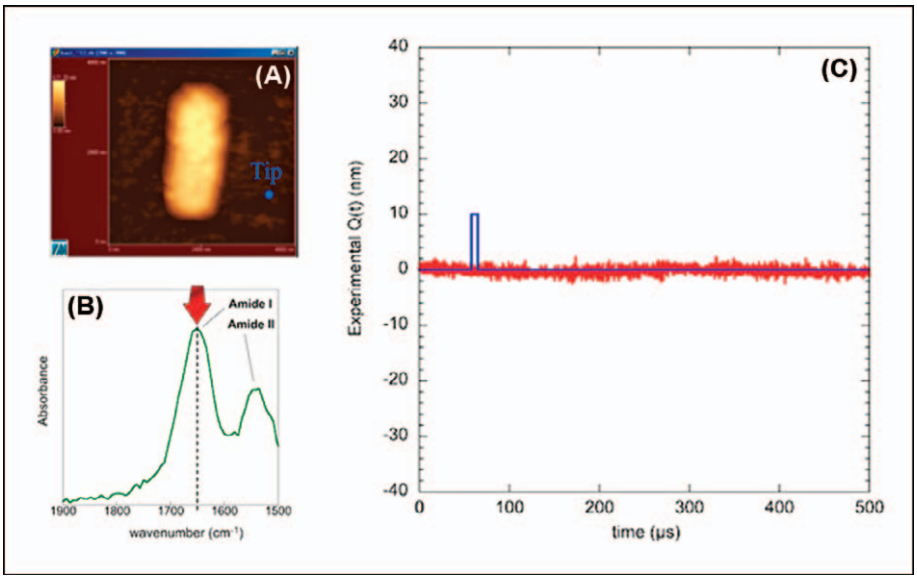

FIG. 3. **(a)** ***AFM topography picture of the bacterium; the position of the tip is indicated in blue.*** **(b)** ***FT–IR absorption spectrum of the bacterium (in green); the wavenumber of the IR laser is indicated by the red arrow.*** **(c)** ***AFM cantilever deflection (in red) as a function of time superposed on the IR pulse laser (blue).***

internal reflection approach in preventing unwanted stray radiation from striking the cantilever.

To test whether the expansion of the bacterium is really related to a specific absorption of bacterium, we tuned the laser wavenumber outside the amide I band to 1800 cm^{-1} (Fig. 4) and put the tip again on the bacterium. The signal showed a small oscillation, not more than 3 nm, which is in good agreement with the relatively small absorption of the bacterium at that wavenumber.

All these experiments have shown that the detected cantilever oscillation is excited by the photothermal expansion of the bacterium. As demonstrated in the Appendix, the amplitude of the cantilever oscillation is directly proportional to the IR absorption. One approach to quantifying the cantilever oscillations is to perform a Fourier analysis of the cantilever oscillation signal. An FFT of the cantilever deflection on and off an absorption band of the bacterium is depicted in Fig. 5. FFT also makes it easy to notice that the thermal expansion pulse excites different cantilever oscillation modes. The strongest mode is the fundamental at a resonance frequency of around 62 kHz. Looking at the maximum of the first mode, we can quantify the amount of absorption in the two different cases.

Figure 6 shows a comparison of an AFM–IR spectrum collected one wavenumber at a time by tuning the laser through the spectral region of interest with a conventional FT–IR spectrum of *E. coli*. While there is significant similarity in the spectra, note that the AFM–IR measurement is performed on a localized region of one bacterium, while the conventional FT–IR represents the average spectrum within a beam area consisting of millions of bacteria.

As mentioned previously, chemical imaging is also possible with the AFM–IR technique. The laser wavenumber is fixed at a value corresponding to a specific IR absorption band originating from a specific molecular vibration of a chemical functional group (e.g., 1660-cm^{-1} amide I, etc.), and the tip is scanned over the sample. The resulting map can show the spatial variation in absorption and hence spatial variation in the concentration of a specific chemical species. Figure 7 shows different chemical maps of *E. coli* for two different bands, amide I (at 1660 cm^{-1}) and amide III (at 1240 cm^{-1}), both characteristic of protein. The band at 1240 cm^{-1} could also contain some contributions from phosphate group absorbances (related to the DNA backbone). In this case, as both IR absorbance images are mainly because of protein, which is distributed homogeneously throughout the *E. coli* cell, the observed signals

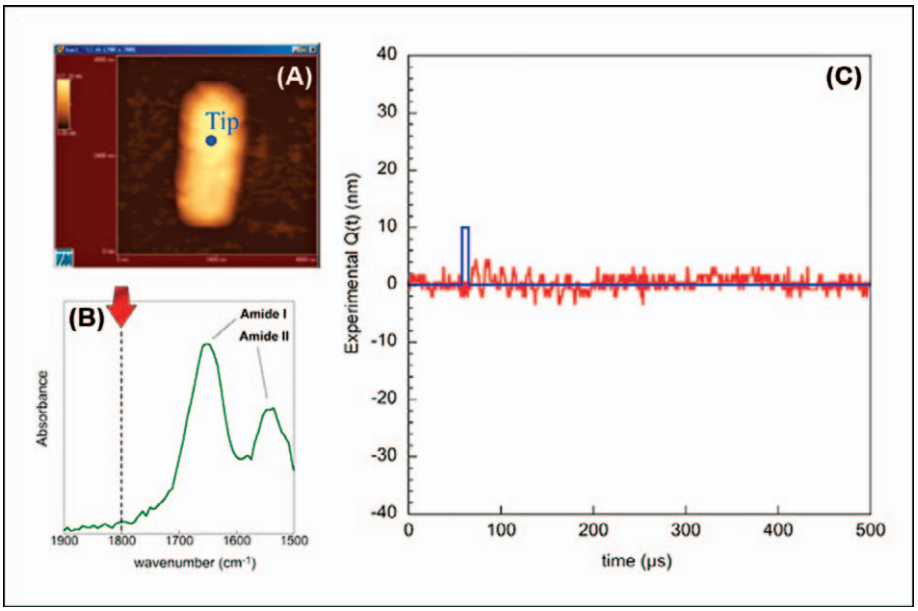

FIG. 4. **(a)** ***AFM topography picture of the bacterium, the position of the tip is indicated in blue.*** **(b)** ***FT–IR spectrum, the bacterium absorption bands is drawn in green, and the wavenumber of the IR laser is indicated by the red arrow.*** **(c)** ***Oscillations recorded by the four-quadrant detector (in red) as a function of time superposed on the IR pulse laser (blue).***

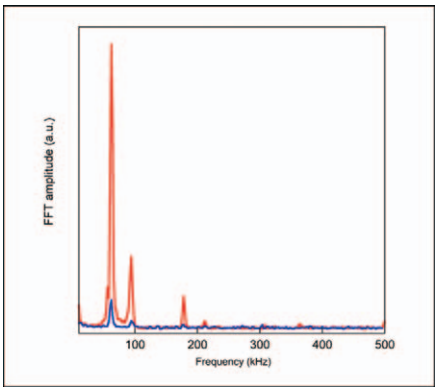

FIG. 5. Fast Fourier transform (FFT) of the cantilever ring-downs of Fig. 2c (red) and Fig. 4c (blue). Note the much larger cantilever oscillation amplitude on the red curve, corresponding to the bacterium absorption at 1650 cm^{-1} vs. the amplitude at 1800 cm^{-1} (blue curve). To obtain an IR spectrum by the AFM–IR technique, one needs only to record the amplitude of a cantilever oscillation mode as a function of the wavenumber of the laser.

were roughly proportional to the AFM topography signal (i.e., related to the sample thickness). The 1660 cm^{-1} absorption was globally more intense than the 1240 cm^{-1} absorbance (ratio of 7:5), which is in good agreement with bulk IR spectroscopy. When the AFM tip was close to the border of the bacterium without touching it, there was no signal. This result illustrates the sensitivity and spatial resolution of the technique. With AFM–IR, it is apparently possible to detect an object with a size approaching a few tens of nanometers. The resolution limitation in the case

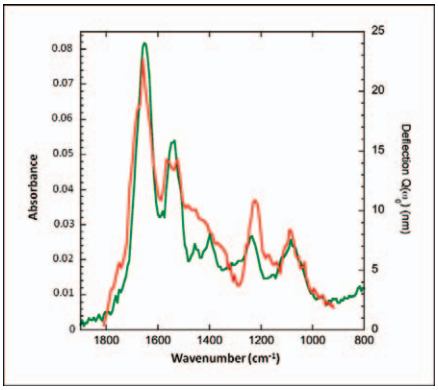

FIG. 6. FT–IR spectrum (in green) of an Escherichia coli culture and AFM–IR spectrum (in red) of a single E. coli bacterium.

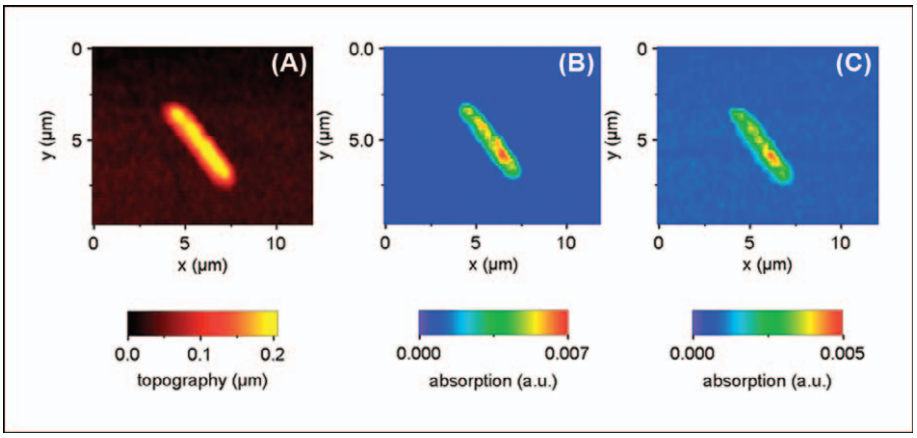

FIG. 7. **(a)** *AFM topography picture of a single bacterium Escherichia coli.* **(b)** *Corresponding chemical mapping of the amide I band (1660 cm^{-1}).* **(c)** *Corresponding chemical mapping of the amide III band (1240 cm^{-1}).*

of an isolated object on the surface is in fact the resolution of the tip itself and the sensitivity of the thermal expansion detection. In the case of non-isolated objects, thermal diffusion can limit spatial resolution.

APPLICATIONS IN POLYMER SCIENCE

AFM–IR is now being used in extensive applications in polymer science. A driving factor is the number and diversity of polymeric materials that incorporate micro- and nanoscale structure to achieve desired properties. Such materials include polymer blends, polymer composites and nanocomposites, and thin films used in both active devices and as passive barriers. This section outlines applications in many of these areas.

Correlation with Conventional FT–IR. One of the first major features of the AFM–IR technique for polymer applications is the strong correlation with measurements by conventional FT–IR spectroscopy. As shown in the Appendix, the signal measured by AFM–IR is directly proportional to the IR absorption coefficient for a material. As such, the absorption spectra are directly related to conventional IR spectroscopy measurements. Figure 8 shows a comparison of AFM–IR and FT–IR measurements on polystyrene, a common reference sample for IR spectroscopy.[32] Note the strong agreement between the two techniques for both the absorption peak positions and band shapes. This correlation allows spectroscopists to directly apply analytical techniques and expertise developed over the last 50 years or more, including the use of extensive material databases for the analysis and identification of unknown components. Databases are available, for example, with the IR spectra of many thousands of polymer compounds.

Improved Spatial Resolution. Another benefit of the AFM–IR technique is to provide spatially resolved measurements of IR absorption spectra on a scale many times smaller than the conventional diffraction limit. This is achieved by virtue of the fact that the AFM tip measures the IR absorption in the extreme near field. Although the IR

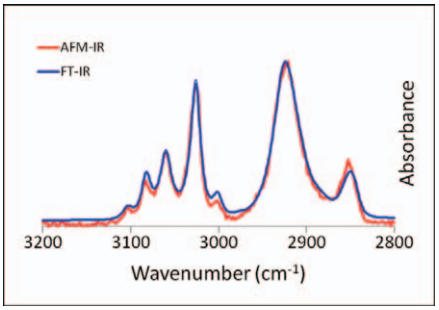

FIG. 8. Comparison of IR absorption spectra of polystyrene in the CH-stretching region by AFM–IR (red) versus FT–IR (blue). Taken with permission from C. Marcott, M. Lo, K. Kjoller, C. Prater, I. Noda. Applied Spectroscopy. 2011. 65(10): 1145–1150. Copyright 2011 The Society for Applied Spectroscopy.

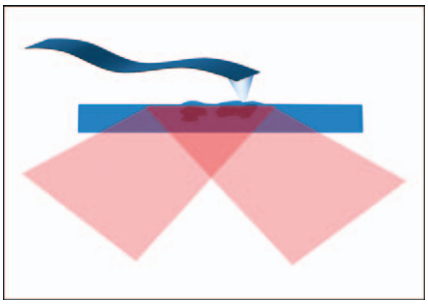

FIG. 9. AFM–IR can achieve spatial resolutions below the diffraction limit, as it measures local variations in thermal expansion because of IR absorption, even if the expanding regions are many times smaller than the incident laser spot.

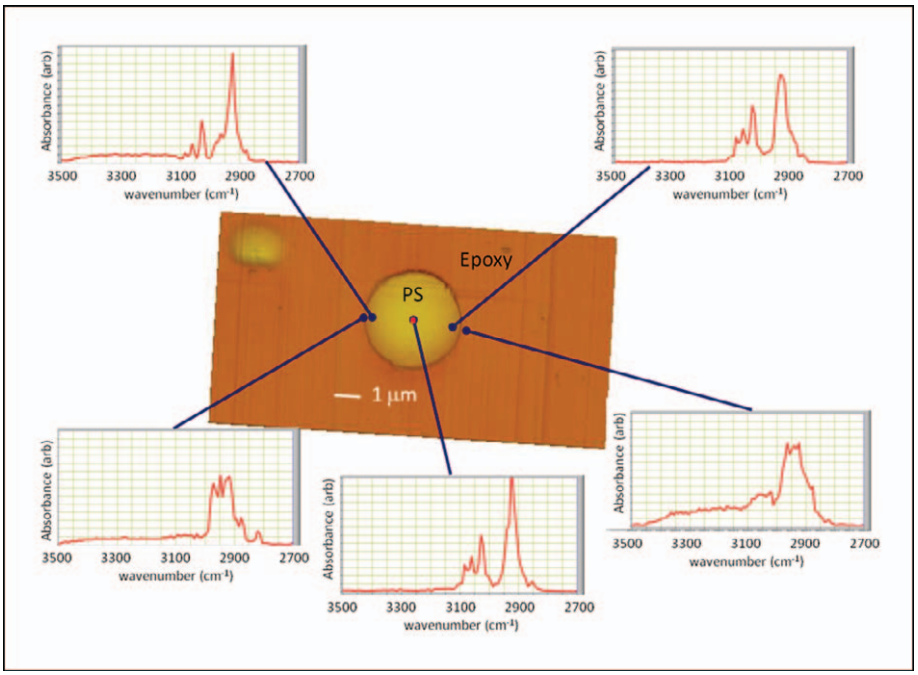

FIG. 10. Demonstration of spatial resolution of the AFM–IR technique on a model polymeric sample. A 3 μm polystyrene (PS) bead was embedded in epoxy and measured with the AFM–IR technique. A spectrum near the middle of the PS bead shows the characteristic aliphatic and aromatic CH stretching bands in the 2800 to 3200 cm^{-1} region. Similar spectra are obtained at the left and right edges of the bead. However, just ~100 nm across the boundary into the epoxy, very different spectra are obtained, characteristic of the absorption spectra of the embedding epoxy. Conventional IR spectroscopy at this wavelength (~3 μm) would have a practical spatial resolution limit of about one to three times the wavelength (depending on technique used), or around 3–9 μm. Thus, a conventional IR microspectroscopy measurement would provide at best spatial resolution equal to the bead size. The approximate spatial resolution of the AFM–IR technique (~100 nm) is shown by the size of the small red square.

laser spot might be limited in size by diffraction, absorbing regions that are smaller than the wavelength will still result in thermal expansions that are smaller that the laser spot size, as illustrated in Fig. 9. The AFM tip can measure this thermal expansion and hence IR absorption with very high spatial resolution.

Figure 10 shows the ability of the AFM–IR to clearly discriminate different materials on the basis of their IR absorption spectra on a length scale at least 30 times finer than conventional IR spectroscopy. The measurement in Fig. 10 shows a series of AFM–IR spectra taken at the center and edges of a polystyrene bead and just across the boundary in neighboring epoxy. The spectra change abruptly on a scale of around 100 nm.

Complementary Mechanical Stiffness Measurements. AFM–IR instrumentation can also be used to obtain complementary measurements of sample stiffness by recording the cantilever contact resonance frequency, as illustrated in Fig. 11. When an AFM tip is in contact with a sample surface, it acts like a coupled spring system (Fig. 11A), where the sample stiffness and damping can be considered similar to a spring–dashpot system. When the AFM–IR laser excites a thermal pulse in the sample, producing oscillations of the cantilever, the resonant frequency is higher on stiff samples and lower on soft samples (Fig. 11B). The contact resonance frequency has an S-shaped dependence on the sample elastic modulus; a model curve is shown (Fig. 11C) for a cantilever style often used in AFM–IR measurements. Measuring this contact resonance frequency as a function of position enables spatially resolved maps of sample stiffness to be generated. Figure 11D shows AFM–IR topography and contact resonance images at the interface between two polymer layers (nylon and an ethylene acrylic acid copolymer) in a multilayer film. Although the topography shows very little contrast, the contact resonance image clearly distinguishes the two polymer materials on the basis of differing elastic modulus.

Figure 12 shows complementary measurements of topography, IR absorption spectra, an IR absorption map, and a stiffness map of another multilayer film. Multilayer films are exceedingly important commercially, being used in applications ranging from food packaging to adhesives to advanced display technologies for computers and mobile devices.

Organic Photovoltaics. The subject of organic photovoltaics is an area of intense international research, with a goal of high efficiency and low-cost generation of electric power. The AFM–IR technique was applied to bulk heterojunctions made of poly(3-hexylthiophene) (P3HT) and [6,6]-phenyl-C_{61}-butyric acid methyl ester (PCBM); an example measurement is shown in Fig. 13. These measurements show spatially varying concentrations of P3HT and PCBM on the basis of characteristic peaks and peak positions associated with the constituent materials. Phase separation of PCBM and P3HT is commonly observed in such polyvinyl blends. In this example, a defect can be seen on the surface in Fig. 13, which shows an AFM image of a heat-treated P3HT–PCBM sample. The methylene bending modes

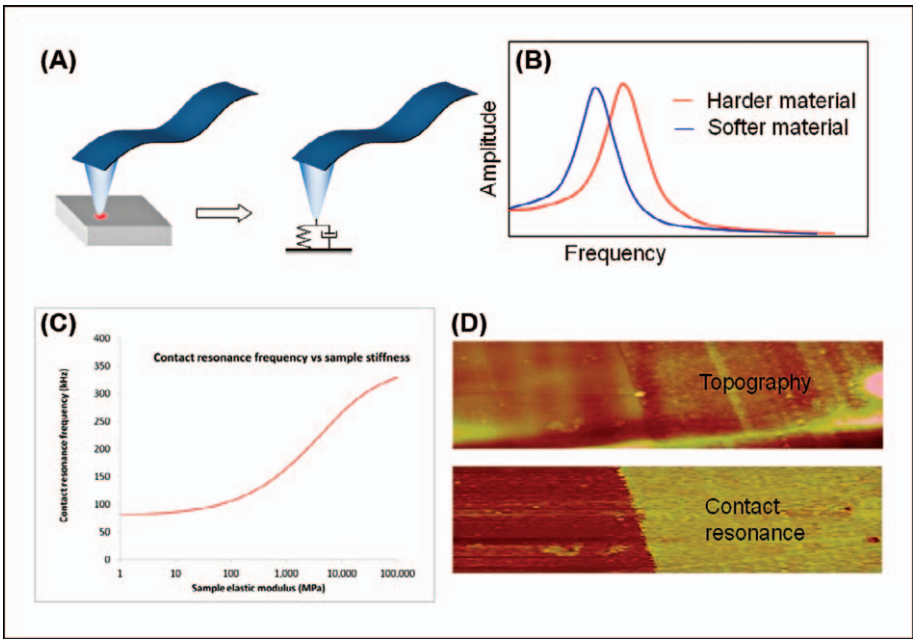

FIG. 11. Illustration of mechanical property mapping with the AFM–IR technique. A cantilever in contact with a sample surface acts like a coupled spring system (A) *wherein the sample elasticity changes the frequency at which the cantilever resonates* (B, C). *Mapping this contact resonance frequency as a function of position* (D) *allows discrimination of materials based on differing stiffness. The images shown in* (D) *are topography (top) and contact resonance frequency (bottom) of an interface region in a polymer multilayer consisting of nylon and an ethylene acrylic acid copolymer.*

at 1444 and 1432 cm^{-1} correspond to P3HT and PCBM, respectively. The 1444 cm^{-1} band also contains a contribution from an overlapping-ring, semicircle stretching mode. The corresponding spectrum for the yellow hash mark appears to have both components. At the outer ring (red mark, spectrum 1), the peak at 1732 cm^{-1} (PCBM) is small, and the component at 1444 cm^{-1} (P3HT) dominates. At both green and purple hash marks (spectra 3 and 4), the band near 1432 cm^{-1} is mainly contributed by PCBM. Finally, the sharpness of the band at 1432 cm^{-1} and a stronger 1732 cm^{-1} signal suggest the lobe at the center is mostly PCBM. By combining the AFM and IR into a single instrument, the topological information is readily correlated with the local chemical analysis. The above data suggest there is local phase separation.

Figure 14 shows a proprietary multicomponent polymer blend. Blends with micro- and nanoscale-sized polymer domains are increasingly common. Often different combinations of polymers are used to achieve desired strength, toughness, and other performance criteria for a specific application. AFM–IR can reveal the spatial distribution of these polymer components and chemically identify polymer constituents.

APPLICATIONS IN MICROBIOLOGY

Location of Poly(hydroxybutyrate) Produced by *Rhodobacter capsulatus*.[26] Poly(hydroxybutyrate) (PHB) belongs to the class of polyesters and has been used for several years for the production of plastics having similar mechanical and thermoplastic properties to those of polyethylene and polypropylene, but with the advantage of biocompatiblity, making it a renewable resource. *Rhodobacter capsulatus* is a purple, non-sulfur, photosynthetic bacterium that produces PHB for energy storage.[33–35] Bacterial PHB is stored in vesicles of variable size, which are degraded by the bacterium when its nutritive resources become limiting. The presence of PHB can be probed in the mid-IR region by detecting one specific absorption band at 1740 cm^{-1} because of the ester C=O stretching vibration, which is easily distinguishable from other bacterial bands (e.g., amides I and II at 1660 and 1550 cm^{-1}respectively).[36] Many studies have been conducted on the characterization of PHB by using different vibrational spectroscopic techniques (e.g., Raman, FT–IR). However, these methods often require prior extraction of PHB[37] and do not allow an in situ study because of the lack

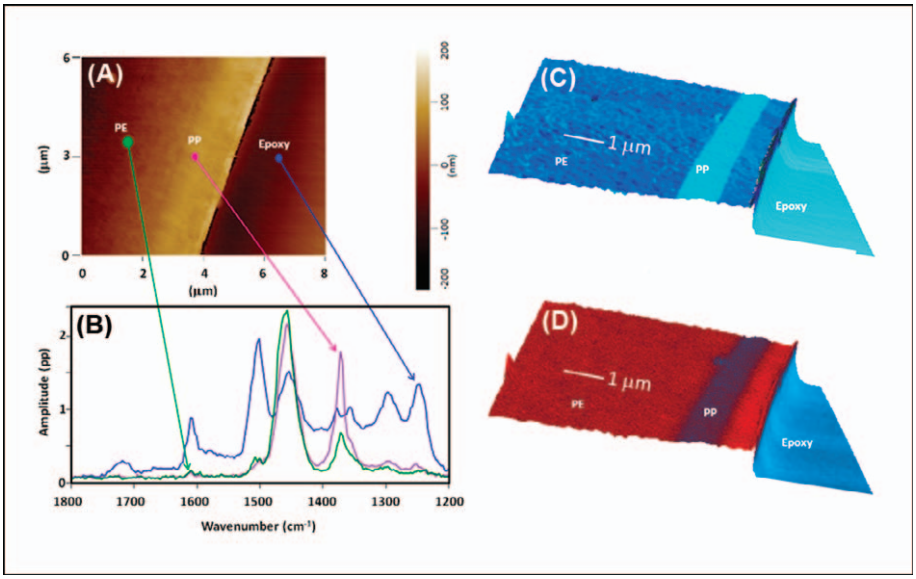

FIG. 12. Multifunctional measurements performed with the AFM–IR on a polymer multilayer film of polypropylene, polyethylene, and embedding epoxy. The measurements show topography (A), *representative IR absorption spectra* (B), *stiffness map* (C), *and an IR absorption image at 1456 cm^{-1}* (D).

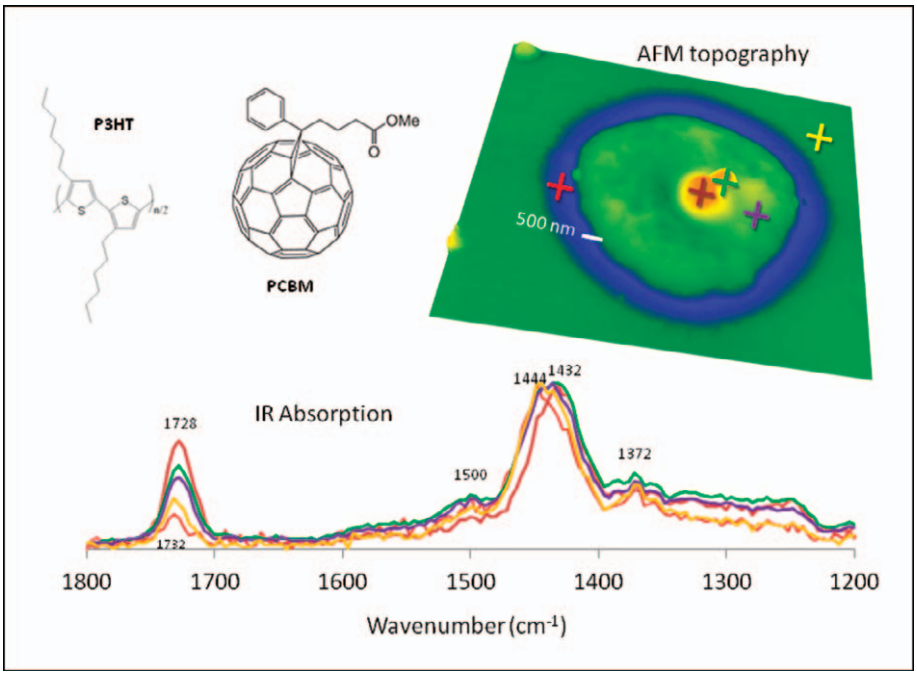

FIG. 13. AFM–IR measurements of bulk heterojunction P3HT–PCBM film. AFM–IR absorption spectra were obtained at several points surrounding a defect observed in the AFM topography image (left). The spectra reveal variations in the amplitude of the carbonyl peak (~1730 cm^{-1}) associated with higher concentration of PCBM. Stronger concentrations of P3HT cause a reduction in the carbonyl peak and a shift in the methylene bending absorption from ~1432 to ~1444 cm^{-1}.

of resolution in imaging. The AFM–IR technique allows the study of PHB directly in the cell without extraction or complex sample preparation.

R. capsulatus wild type was grown under classical conditions. The cell suspension was spun down by centrifugation at 1000 rpm for 15 min. The supernatant was removed, and the pellet was diluted in distilled water. A drop of the solution was deposited on the ZnSe prism for AFM–IR studies or on ZnSe glass for FT–IR and dried at room temperature for 20 min.

The top panels in Fig. 15 display the AFM topography of *R. capsulatus*. The variations in height are given a red–yellow color code, where the maximum is represented by the yellow. The bottom panels represent the amplitude distribution of the cantilever fundamental mode, with the laser wavenumber tuned at 1740 cm^{-1}, which corresponds to the chemical cartography of ester C=O stretching vibration (specific band of PHB), on a rainbow scale. The scale indicates increasing absorption when the signal shifts from purple to red. On all maps, round red areas are apparent. These domains correspond to PHB granules inside the bacterium (Figs. 15d through 15f). On each map, it is possible to estimate the size of granules by taking the width at half height.[26] For a dozen measurements, we observed round shape sizes in the range of 100 to 400 nm, which is consistent with the transmission electron microscopy (TEM) studies of the same culture made jointly.[26]

Figure 15d reveals a 210 nm diameter round granule and, and an oval-shaped one only 50 nm across (top of the image). This oval shape could correspond to an alignment of small vesicles initially produced by the bacterium membrane.[38] Figure 15e shows one bacterium with, and another without, a PHB vesicle. This suggests that under these growing conditions, all *R. capsulatus* cells do not necessarily produce PHB. The PHB-to–bacteria volume ratio is low by looking at our chemical mapping. This is in good agreement with the FT–IR spectrum of the bacteria culture (Fig. 16a, green curve), where the ester carbonyl band appears as a shoulder on the amide I band. Figure 15f (zoom of Fig. 15e) shows more clearly that the absorbing area is in fact composed of two adjacent vesicles of different sizes.

One must be careful when interpreting AFM–IR chemical images alone, because the contrast can come not only from IR absorption, but also from thermomechanical artifacts because of the sample mechanical properties. To prove that the mapping contrast really results from chemical differences, we recorded the spectroscopic response of the one vesicle and compared it with the FT–IR spectrum of the bacteria culture in Fig. 16.

The spectrum on a single bacterium (in red in Fig. 16a) was measured by

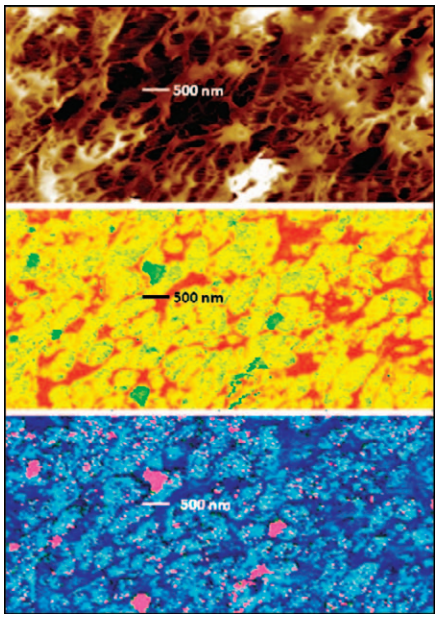

FIG. 14. AFM–IR measurements of a polymer blend, including topography image (top), IR absorption at 1450 cm^{-1} (center), and stiffness map (bottom). While the topography image reveals intricate morphology, it gives only limited clues about the chemical and mechanical properties of the sample. The IR absorption map (center) and stiffness map (bottom) clearly resolve three different constituents in this polymer blend. Note for example the three shades of green, yellow, and orange in the absorption image (center) image and the three different shades of pink, light blue, and dark blue in the stiffness map (bottom).

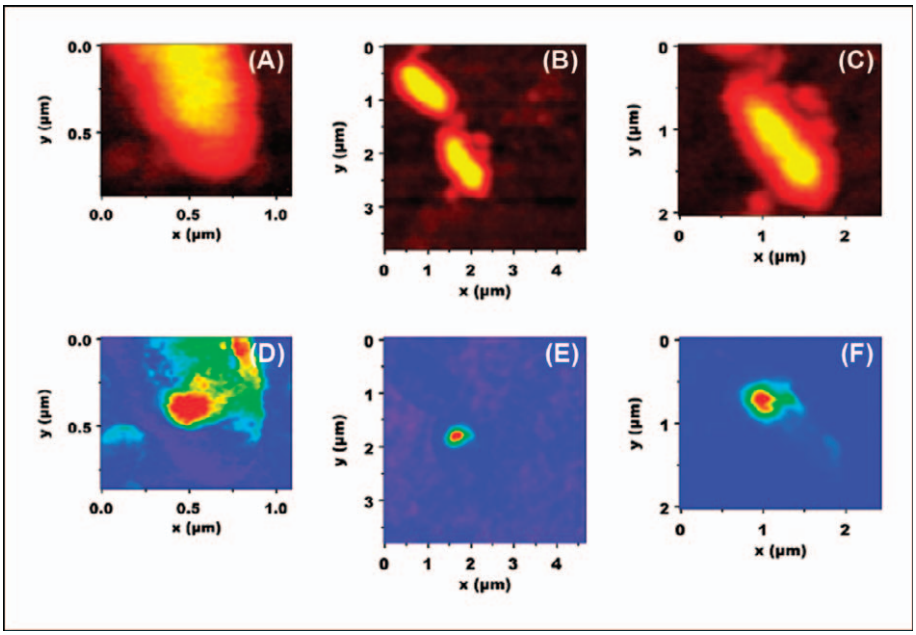

Fig. 15. **(a)** ***AFM topography of a single Rhodobacter capsulatus.*** **(b)** ***AFM topography of two separated R. capsulatus bacteria.*** **(c)** ***AFM zoom on the lowest bacterium localized on*** **(b). (d)** ***Chemical mapping of PHB (at 1740 cm^{-1}) of the corresponding topography*** **(a). (e)** ***Chemical mapping of PHB of*** **(b). (f)** ***Chemical mapping of PHB of*** **(c).**

positioning the tip of the AFM directly on the maximum of the signal by using the chemical mapping of PHB (as indicated by point A in Fig. 16b). We observe an intense PHB ester carbonyl stretching band (centered at 1740 cm^{-1}), whereas the amide I band at 1660 cm^{-1} appears weaker. As the tip is positioned directly over the vesicle, there is no amide I IR absorbance signal. However, there are many proteins surrounding the PHB vesicle, which can generate a small response in the amide I spectral region. Concerning the C=O stretching band of the ester, we obtained a clear signal demonstrating that PHB is almost certainly responsible for the hot spots observed on the 1740 cm^{-1} maps shown in Figs. 15 and 16. The second spectrum (B) shown in Fig. 16a was recorded by positioning the tip at point B in Fig. 16b at the border of the vesicle indicated in the 1740 cm^{-1} absorption image. The spectrum shows a better signal for the amide I that is similar to the FT–IR spectrum of the bacteria culture (Fig. 16a in green). The intensity of the PHB C=O ester band in that case has decreased compared with position A, which is consistent with the PHB chemical mapping. When the tip is moved to position C (Fig. 16b), out of the vesicle, the AFM–IR spectrum does not show the C=O band (in violet, Fig. 16a). The behavior of the spectra is in good agreement with the contrast of the chemical mapping. This confirms that the AFM–IR technique gives us realistic mapping and IR spectra at spatial resolutions <100 nm.

Characterization of Microdomains in Poly(hydroxyalkanoate) Copolymer Films. As described above, polyhydroxyalkanoates (PHAs) are a class of polyesters that can be accumulated as energy-storing granules in the cells of certain microorganisms such as *R. capsulatus*. A reason one of the most common PHA polymers, PHB, has not proven a feasible polyolefin replacement is because the material is stiff and brittle because of its high degree of crystallinity, and it can become thermally unstable during processing. This shortcoming has led to efforts to copolymerize PHB with other co-monomers to improve its mechanical properties.[39–41] Poly(3-hydroxybutyrate-*co*-3-hydroxyhexanoate) [P(HB-*co*-HHx)], with a melting temperature of 110 to 160 °C and 35 to 45% crystallinity, is a typical available grade, and its morphology was explored using AFM–IR.[32]

Thin films of P(HB-*co*-HHx) were studied in the bulk by IR transmission spectroscopy in an attempt to understand how a thermally induced phase transition affects the molecular structure of the material.[42] Significant spectral changes were observed in both the carbonyl ester stretching region (1770−1670 cm^{-1}) and the C−O−C backbone stretching region (1400–1200 cm^{-1}). The spectral changes observed as the temperature was increased from 30

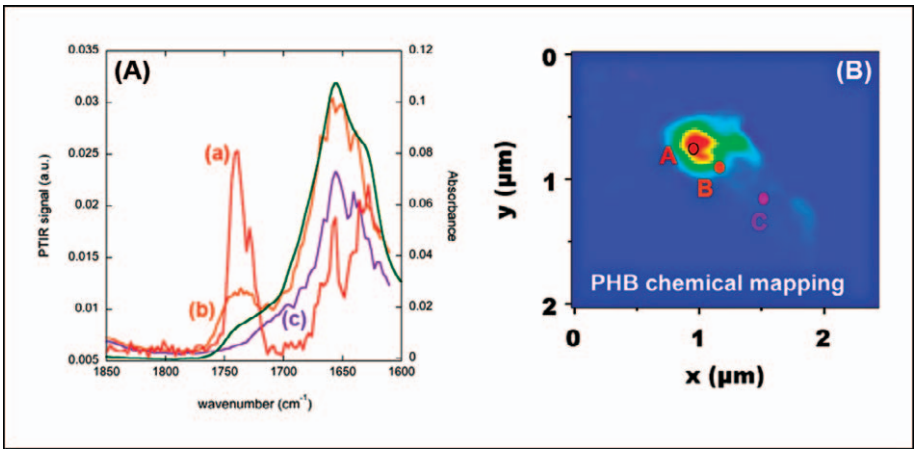

Fig. 16. **(a)** ***Comparison between local AFM–IR spectra (A in red, B in orange, C in violet) and a corresponding FT–IR spectrum (in green) of the bacteria culture.*** **(b)** ***Bacterium chemical mapping of the ester C=O stretching band showing the specific locations of the AFM–IR spectral measurements*** **(A–C).**

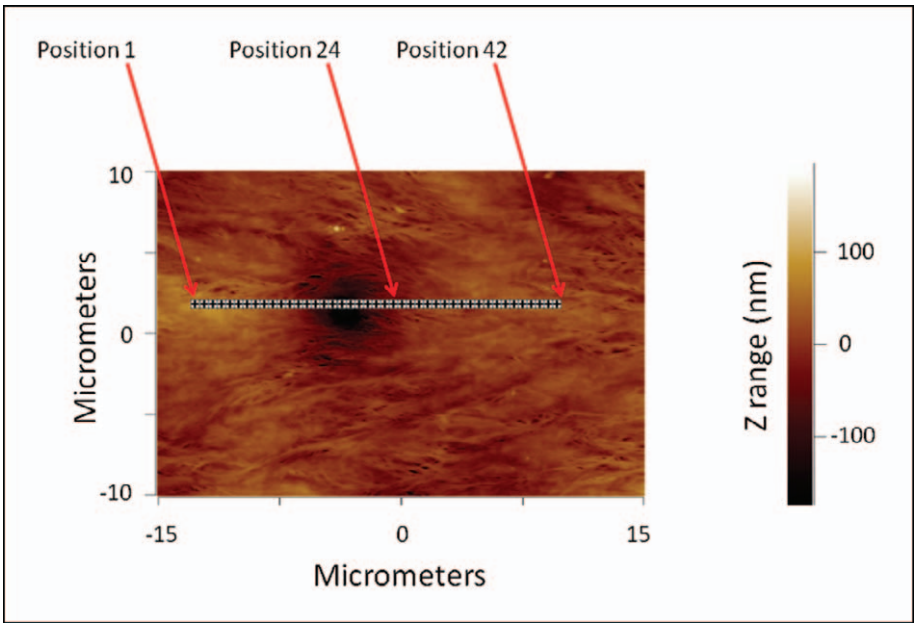

FIG. 17. AFM height image of P(HB-co-HHx) showing a line scan of 42 positions, 200 nm apart, where individual AFM–IR spectra were collected. Position 24 is just left of the dark area (hole) on the AFM image where the sample was locally heated and allowed to cool before measurement. Taken with permission from C. Marcott, M. Lo, K. Kjoller, C. Prater, I. Noda. Applied Spectroscopy. 2011. 65(10): 1145–1150. Copyright 2011 The Society for Applied Spectroscopy.

to 140 °C clearly reflected changes in the polymer conformational structure.[42] Akin to polyethylene and polypropylene, P(HB-*co*-HHx) materials are semicrystalline, which means films formed from them usually contain both crystalline and disordered (amorphous) domains at room temperature. The size and morphology of the resulting microdomains depend critically on the processing conditions used to form them, as well as the sample history. Conventional FT–IR microspectroscopy typically does not have the ability to spatially resolve and spectrally identify individual microdomains.

Figure 17 shows an AFM topography image of a 450 μm-thick P(HB-*co*-HHx) sample film, whereon an AFM tip heated to 350 °C was brought to within 3 μm of a spot slightly above and left of the center of the image for 90 s. The heated tip produced a "hole" in the sample film, as indicated by the dark area in the image. A series of 42 individual AFM–IR spectra were collected after the sample cooled back to room temperature, along the line shown.[32] The spectrum recorded at position 24, just to the right of the hole produced by the heated tip, represented the most well-ordered (crystalline) environment of the carbonyl functional group. Figure 18 shows a stack plot of the expanded regions of the AFM–IR spectra between 1770 and 1670 cm^{-1} (left) and between 1400 and 1200 cm^{-1} (right) of spectra 24 to 36.[32] The spectra in the carbonyl stretching region (left) indicate the presence of three bands, two overlapped bands at 1720 cm^{-1}, and a third broader band at 1740 cm^{-1}. It is clear that the carbonyl intensity is gradually shifting from the two overlapped bands at 1720 cm^{-1} to the broader feature at 1740 cm^{-1} as one progresses from spectrum 24 to 36. This spectral progression provides insights into how this polymeric system recrystallizes after the heated AFM tip produced a nucleation site in the sample film. The most crystalline structure, as indicated by the carbonyl band, appears at the edge of the heated area, and the sample apparently becomes progressively more disordered as a function of distance from this point in a direction away from the nucleation site. The corresponding changes in the C–O–C backbone stretching region near 1276 cm^{-1} are much more dramatic and more difficult to unambiguously interpret at the molecular level. It is intriguing that the behavior of the of the C=O region AFM–IR band-shape change relative to the C–O–C backbone

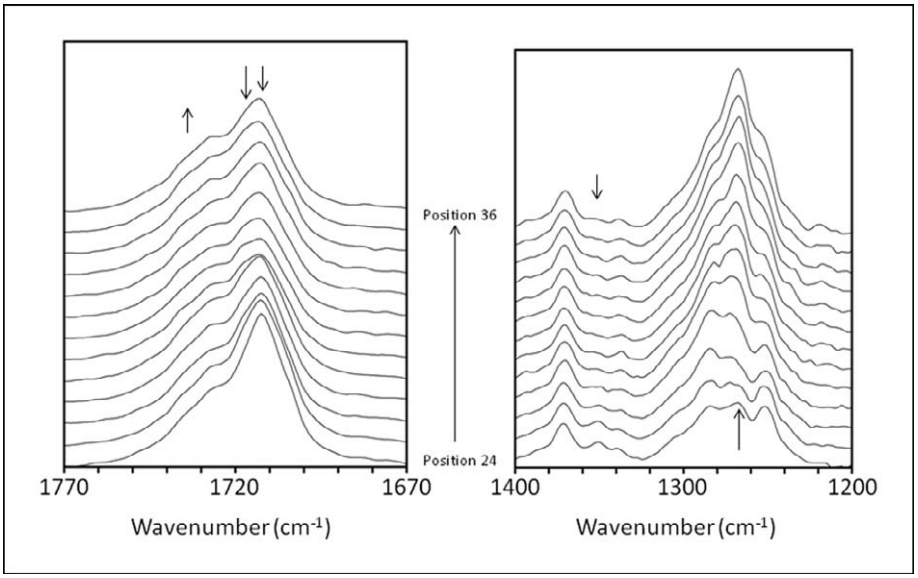

FIG. 18. AFM–IR spectra of P(HB-co-HHx) from positions from 24 to 36 on Fig. 17. Bands associated with more ordered (crystalline) structure decrease in intensity, while bands associated with less ordered (amorphous) structure increase in intensity as one moves from position 24 to 36. Taken with permission from C. Marcott, M. Lo, K. Kjoller, C. Prater, I. Noda. Applied Spectroscopy. 2011. 65(10): 1145–1150. Copyright 2011 The Society for Applied Spectroscopy.

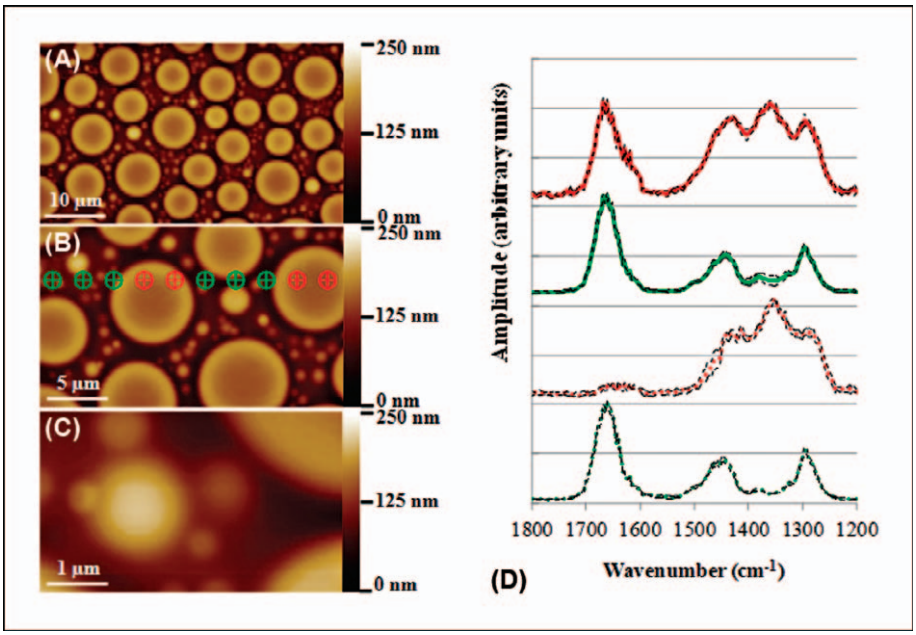

FIG. 19. Localized nanoscale mid-IR spectra of a DEX40-PVP90 blend. **(A–C)** ***Topographical images (the positions of the spectral measurements are marked; the distances between measurement locations are about 2.5 μm).*** **(D)** ***Average local nanoscale mid-IR spectra (1200–1800 cm^{-1}, normalized and offset). From bottom to top: pure PVP90 (n = 10, green dotted line), pure DEX40 (n = 10, red dotted line), PVP-rich phase in the DEX40-PVP90 blend (n = 6, green solid line), and DEX-rich phase in the DEX40-PVP90 blend (n = 4, (red solid line). Black dashed spectra in*** **(D)** ***are those of the average ± standard deviation. Adapted with permission from B. Van Eerdenbrugh, M. Lo, K. Kjoller, C. Marcott, L.S. Taylor. Molecular Pharmaceutics. 2012. 9: 1459–1469. doi:10.1021/mp300059z. Copyright 2012 The American Chemical Society.***

region band-shape change is exactly opposite of the bulk IR measurements recorded as a function of temperature.[42] This suggests that collecting a bulk IR spectrum at higher temperature might not necessarily be representative of the situation in a non-crystalline region of a particular microdomain at room temperature. Thus, the ability to record IR spectra at sub-micrometer spatial resolutions could revolutionize the way we think about the molecular conformations in microdomains of semicrystalline polymers.

MISCIBILITY IN PHARMACEUTICAL BLEND FORMULATIONS

Determining the extent of miscibility of amorphous components is of great importance for certain pharmaceutical systems, in particular for polymer–polymer and polymer–small molecule blends. For amorphous solid dispersions, where an amorphous drug is intimately mixed with a polymeric carrier, formation of miscible systems is desired as it increases the physical stability of the system. Two model systems for polymer–polymer[43] and drug–polymer[44] miscibility were examined and are reviewed below.

Dextran–Poly(vinylpyrrolidone) Blends. Blends of dextran (DEX) and poly(vinylpyrrolidone) (PVP) have been used extensively as model systems for the study of polymer–polymer miscibility. The miscibility characteristics of a set of 50:50 (wt/wt) polymer blends composed of PVP and DEX of varying molecular weights were investigated.[43] Although differential scanning calorimetry (DSC) is usually considered the standard technique for evaluating miscibility behavior in pharmaceutical blends, a number of issues have been identified with the technique over the years. Typically, a single glass transition (T_g) is expected for a miscible blend, but sometimes identification of all glass transitions in a thermogram can be difficult in cases where the pure components of a mixture have very similar T_g values. In addition, a minimal domain size (e.g., 10 to 50 nm for polymeric blends) is typically required for phase-separated domains to produce distinguishable T_g events.[45,46] The width and/or heat capacity changes associated with a glass transition event might also be too broad or weak to allow for its identification.

One particular 50:50 PVP–DEX blend system is presented here to illustrate the power of AFM–IR to provide spatially resolved insights into the morphology of the blend.[43] Specifically, PVP90 (MW = 1–1.5 MDa) and DEX40 (MW = 40 kDa) were prepared by mixing equal amounts of 10% (wt/vol) aqueous solutions of the pure components. This particular blend system was determined to be immiscible by DSC. A thin film was formed on the surface of a ZnSe prism by spin coating 100 μL of the polymer blend solution for 20 s at 3100 rpm, which was subsequently evaluated by nanoscale mid-IR spectroscopy by using a nanoIR™ AFM–IR instrument (Anasys Instruments). All data were obtained in contact mode with a three-lever cantilever (CSC37-ALBS, Mikromasch, Tallin, Estonia). The IR laser produced 10 ns pulses at a repetition rate of 1 kHz. The power levels incident on the ZnSe prism were ~0.5 mW, and the focused laser spot size was about 50 μm at the sample surface. Local spectra were collected over a 1200 to 1800 cm^{-1} spectral range by using a data point spacing of 4 cm^{-1} and the spectral resolution as determined by the laser line width was ~8 cm^{-1}. A total of 128 scans were co-added for each data point in a given spectrum. IR images of the DEX40-PVP90 system were collected at both 1280 and 1350 cm^{-1}, with a contact frequency of 137 kHz and a width of 20 kHz. The images 25 × 15 μm^2 presented correspond to an array of 512 × 64 measurements. Thus, the spacing between points was about 50 nm on the x axis and about 225 nm on the y axis. Once again, a total of 16 cantilever ring downs were co-added at each spatial location. The raw data of the spectral images were further processed with Gwyddion (version 2.19, http://

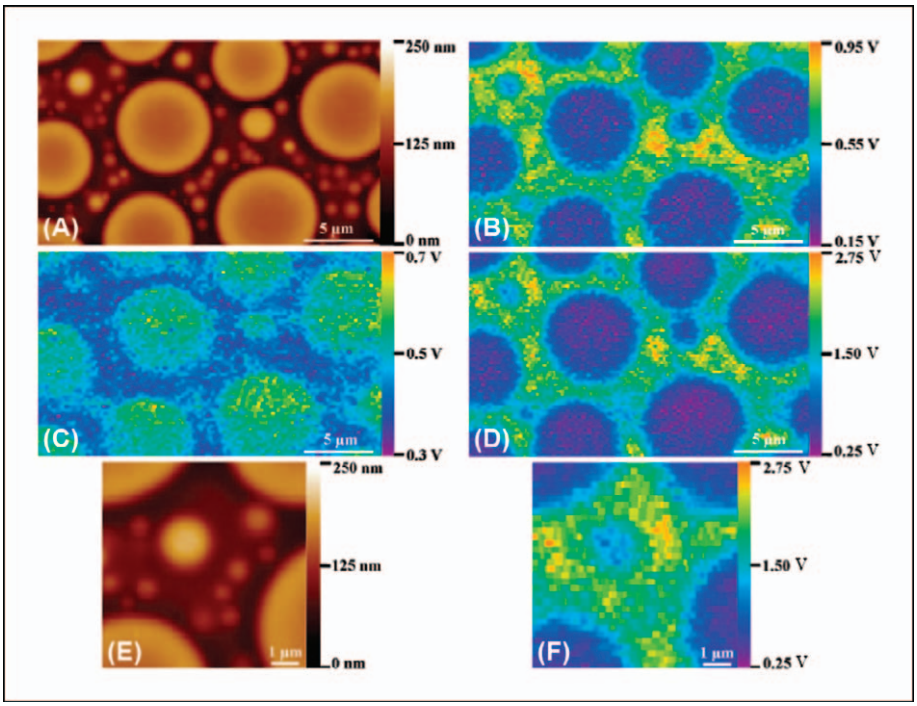

FIG. 20. Nanoscale mid-IR mapping of the DEX40-PVP90 system. **(A)** *Topographical image.* **(B)** *Mapping image at 1280 cm^{-1}.* **(C)** *Mapping image at 1350 cm^{-1}.* **(D)** *Ratio image (1280:1350 cm^{-1}).* **(E)** *Magnification of the topographical image.* **(F)** *Magnification of the ratio image of 1280:1350 cm^{-1}. Adapted with permission from B. Van Eerdenbrugh, M. Lo, K. Kjoller, C. Marcott, L.S. Taylor. Molecular Pharmaceutics. 2012. 9: 1459–1469. doi:10.1021/mp300059z. Copyright 2012 The American Chemical Society.*

gwyddion.net/). Ratio images were constructed by dividing the intensities of the map obtained at 1280 cm^{-1} by those collected at 1350 cm^{-1}.

Standard AFM imaging confirms the formation of a phase-separated blend (Figs. 19A through 19C), in agreement with the DSC results.[43] Discrete domains with diameters of 5 to 10 μm are distributed within a thinner continuous phase (Figs. 19A and 19B). The continuous phase also contains smaller, discrete domains with diameters ranging from about a few hundred nanometers to a few micrometers (Figs. 19B and 19C). Nanoscale mid-IR spectral measurements performed at select locations are shown in Fig. 19B. These spectra (Fig. 19D) show that thicker, DEX-rich discrete domains are distributed in a PVP-rich continuous phase. Figures 20A through 20F show IR images of the same DEX40-PVP90 sample collected with the fixed laser wavenumbers of 1280 and 1350 cm^{-1}.[43] These wavenumbers were selected because pure DEX absorbs more strongly at 1350 cm^{-1} than it does at 1280 cm^{-1}, while the opposite is true for PVP. The image generated by evaluating peak intensity variations at 1280 cm^{-1} (Fig. 20B) shows higher intensities for the continuous phase, while in the 1350 cm^{-1} image (Fig. 20C), the discrete domains have higher intensities.[43] These results are consistent with the formation of DEX-rich domains within a PVP-rich continuous phase. As local topography and mechanical properties can also influence the spectroscopic intensities measured in single-wavelength images, it is good practice to confirm the interpretation by generating ratio images.[43,44] When the ratio image of 1280:1350 cm^{-1} (shown in Fig. 20D) is compared with the topographical image in Fig. 20A, it is once again clear that the large discrete domains correspond to a DEX-rich phase, while the continuous phase is rich in PVP. Figures 20E and 20F show the topographical and ratio images of the upper left-hand corner of Figs. 20A through 20D, with additional magnification.[43] It is clear that the sub–micrometer-sized discrete domains present in the continuous phase have lower band ratios (blue regions) compared with those of the continuous phase, indicating that these smaller discrete domains are also DEX rich

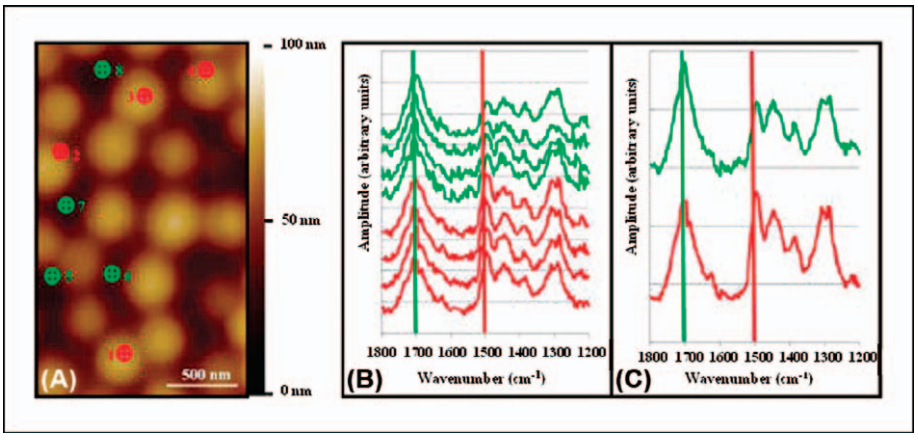

FIG. 21. Localized nanoscale mid-IR spectra of a 50:50 (wt/wt) felodipine–PAA system obtained at discrete domains (1–4) and in the continuous phase (5–8). **(a)** *Topographical image (1.5 × 2.5 μm^2, color scale is 100 nm, the positions of the spectral measurements are marked),* **(b)** *nanoscale mid-IR spectra (1200–1800 cm^{-1}, spectra from bottom to top corresponds to locations 1–8, normalized and offset), and* **(c)** *average spectra of both phases (1 to 4 bottom, 5 to 8 top, n = 4, normalized and offset). Adapted with permission from B. Van Eerdenbrugh, M. Lo, K. Kjoller, C. Marcott, L.S. Taylor. Journal of Pharmaceutical Sciences. 2012. 101(6): 2066–2073. doi:10.1002/jps.23099. Copyright 2012 Journal of Pharmaceutical Sciences.*

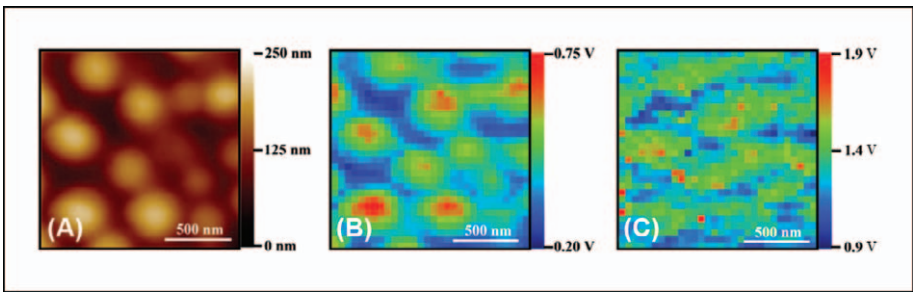

FIG. 22. Nanoscale mid-IR mapping of a 50 : 50 (wt/wt) felodipine–PAA system (1.5 × 1.5 μm²). (a) *Topographical image (color scale is 250 nm),* (b) *spectroscopic image obtained at 1500 cm⁻¹ (color scale is 0.20–0.75 V),* (c) *image ratio of 1 500:1 700 cm⁻¹ (color scale is 0.9 to 1.9). Adapted with permission from B. Van Eerdenbrugh, M. Lo, K. Kjoller, C. Marcott, L.S. Taylor. Journal of Pharmaceutical Sciences. 2012. 101(6): 2066–2073. doi:10.1002/jps.23099. Copyright 2012 Journal of Pharmaceutical Sciences.*

and provide further demonstration of the sub-micrometer chemical imaging capabilities of the technique.[43]

Felodipine–Poly(acrylic acid) Blends. The state of dispersion of an active pharmaceutical ingredient (API) in a polymeric carrier can have a major impact on its release kinetics, strongly influencing the effectiveness of the drug. Dispersions of APIs with polymers can be on a molecular, nanometer, or micrometer scale, or some combination thereof. Manufacturing conditions and formulation variables are important factors influencing the polymer and drug domain sizes and phase behavior. In addition, the state of drug dispersion can change over time, either during storage or on drug release.[44]

A model drug–polymer blend system composed of felodipine and poly(acrylic acid) (PAA) was examined with AFM–IR.[44] When prepared as an amorphous solid by solvent evaporation, felodipine has relatively low crystallization tendency;[47,48] therefore, it serves as a good model compound to evaluate drug–polymer miscibility, because it can be assumed that the drug will remain amorphous. PAA is an amorphous polymer that does not crystallize. This particular drug–polymer combination appears to be miscible at low and high polymer concentrations, but phase separation is observed at intermediate compositions.[44] An AFM height image and local nanoscale mid-IR spectra obtained on a 50:50 (wt/wt) felodipine–PAA blend system are shown in Fig. 21.[44] The average thickness of the film was approximately 570 nm. Locations where spectra were taken are marked on the images and correspond to discrete domains (1–4, marked in red) and the continuous phase (5–8, marked in green). As can be seen from the individual spectra (Fig. 21b) and their averages (Fig. 21c), clear spectral differences can be observed, depending on the region of the system probed, particularly when comparing the intensity of the peak at around 1700 cm^{-1} with that found at 1500 cm^{-1}.[44] For the continuous phase, the peak at around 1700 cm^{-1} is the dominant peak in the 1200 to 1800 cm^{-1} spectral region compared with the peak at 1500 cm^{-1}. For the discrete domains, peak intensities at 1500 cm^{-1} tend to be somewhat higher than those obtained at 1700 cm^{-1}.

The IR bands at 1500 and 1700 cm^{-1} were selected for imaging purposes because of their ability to discriminate between the felodipine and PAA components of the bend. Figure 22 shows images collected with the tunable laser source tuned to these two wavenumbers.[44] Good correspondence is observed between the image obtained at 1500 cm^{-1} (Fig. 22b) and the topographical image (Fig. 22a). Rather than drawing conclusions based on measurements made at a single wavenumber, it is prudent to examine the relative differences in response by using images collected at multiple wavenumbers. Figure 22c shows an image generated by taking the ratio of the responses at 1500 and 1700 cm^{-1}.[44] The blue regions have a propensity to correspond to the PAA-rich continuous phase, while green and red regions correspond to the felodipine rich discrete domains.

MOLECULAR ORIENTATION IN ELECTROSPUN FIBERS

Electrospinning has established itself as an efficient technique to produce small-diameter (10 nm to 10 μm) polymer fibers. The fibers are fabricated from polymer solutions or melts by using an applied electric field. Many polymers were successfully electrospun, and their applications include composites, filtration systems, medical prosthesis, tissue templates, electromagnetic shielding, and liquid crystal devices.[49]

Poly(vinylidene fluoride). There is considerable interest in electrospun fibers of poly(vinylidene fluoride) (PVDF) because of its piezoelectric and pyro-electric properties. Electrospun fibers of PVDF in the β phase were recently characterized by a variety of techniques, including by scanning electron microscopy, polarized FT–IR spectroscopy, TEM, and selected area electron diffraction.[50] The nanofibers in this case were collected on aluminum foil across a 10 μm gap in order to get them to align so polarized FT–IR measurements could be performed, as the width of an individual fiber was well below the diffraction limit of the IR light used to make the measurement. These measurements are important because they provide key information about the molecular orientation of the polymer chains within the fibers, which affects their properties. Without the capability to perform sub–diffraction-limited polarized IR spectroscopy on an individual nanofiber, it was necessary to collect polarized FT–IR transmission on a multiple fibers that were forced to be roughly aligned across the 10 μm gap. Although a useful compromise, the fibers were not all 100 percent aligned in exactly the same direction. This made it difficult to determine with certainty if any orientation relaxation that might have occurred in an electrospun fiber mat was because of fiber rearrangement or relaxation in the individual nanofibers.

Even though the laser source of the AFM–IR instrument is polarized in some direction, up to now, we have

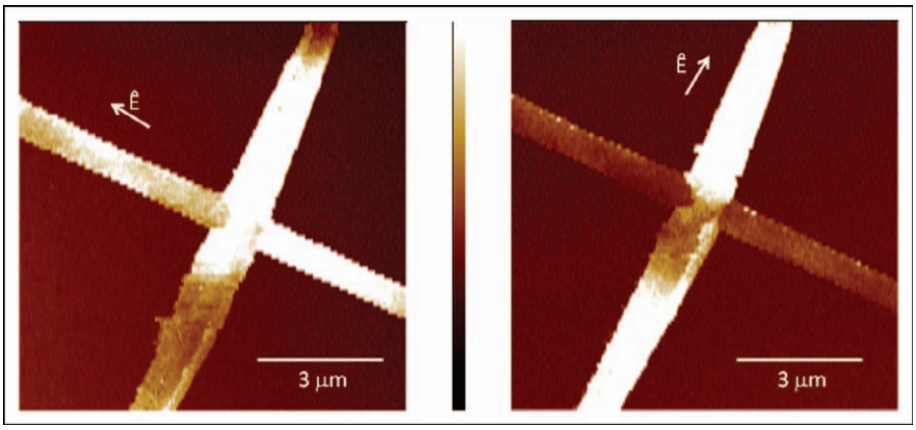

FIG. 23. IR absorbance images of two PVDF fibers collected with the pulsed laser source tuned to 1404 cm^{-1} by using light polarized in the two orthogonal directions indicated. Lighter color indicates stronger absorbance at that wavenumber.

not taken advantage of this to add potentially valuable molecular orientation information to what was discussed so far in this review. For this PVDF-oriented nanofiber characterization study, a device enabling arbitrary angle, broad-band control of the polarization was added to the AFM–IR instrument (nano-IR, Anasys Instruments).

Figure 23 shows two IR absorbance images on two roughly perpendicular electrospun PVDF fibers approximately 1 μm in diameter. The images were recorded with two different polarizations with the pulsed-laser illumination fixed at 1404 cm^{-1}, the wavenumber of one of the stronger PVDF absorption bands. The results clearly indicate that the electric dipole-transition moment of this IR band, due to CH_2 wagging and C–C anti-symmetric stretching vibrational motions, was aligned along the fiber axis.

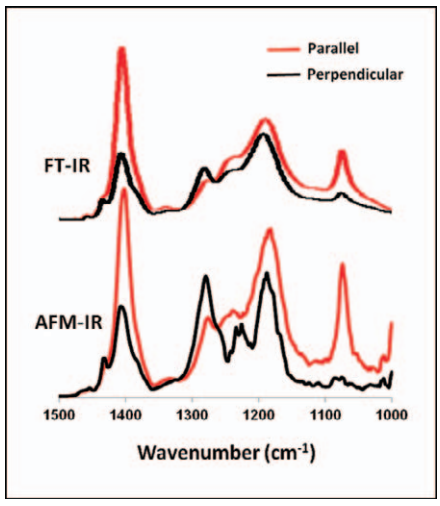

FIG. 24. Two polarized AFM–IR spectra **(bottom)** *collected from the same single location on one of the fibers shown in Fig. 23. For comparison, two averaged polarized FT–IR spectra of multiple aligned fibers are shown at the top.*

Figure 24 shows two polarized AFM–IR spectra (bottom) collected from the same single location on one of the fibers shown in Fig. 23. For comparison, two averaged-polarized FT–IR spectra of multiple aligned fibers are shown at the top of Fig. 24. The excellent agreement between these two measurements demonstrates that we should now be able to use AFM–IR spectroscopy to examine the molecular structure and orientation at multiple locations on individual nanofibers.

CONCLUSION

We have demonstrated the broad utility of the AFM–IR technique in the material and life sciences. We showed that there is excellent agreement between AFM–IR and conventional IR spectroscopy measurements, allowing significant leverage of existing expertise in IR spectroscopy. In addition, we showed how the AFM–IR technique can be used to acquire IR absorption spectra and absorption images with spatial resolution on the 50 to 100 nm scale versus the scale of many micrometers or more for conventional IR spectroscopy. This review also summarizes several applications of AFM–IR in the life and polymer sciences. In the life sciences, experiments demonstrated the ability to perform chemical spectroscopy at the sub-cellular level. Specifically, the AFM–IR technique provides a label-free method for mapping IR-absorbing species in biological materials. On the polymer side, AFM–IR was used to map the IR absorption properties of polymer blends, multilayer films, thin films for active devices such as organic photovoltaics, microdomains in a semi-crystalline polyhydroxanoate copolymer, as well as model pharmaceutical blend systems. The ability to obtain spatially resolved chemical spectra as well as high-resolution chemical images collected at specific IR wavenumbers was demonstrated. Complementary measurements mapping variations in sample stiffness were also obtained by tracking changes in the cantilever contact resonance frequency. Finally, it was shown that by taking advantage of the ability to arbitrarily control the polarization direction of the IR excitation laser, it is possible to obtain important information regarding molecular orientation in electrospun nanofibers.

ACKNOWLEDGMENTS

We gratefully acknowledge the many collaborators who have provided samples and/or measurements described in this review. We specifically recognize Kevin Kjoller, Michael Lo, Debra Cook, Greg Meyers, Céline Mayet, Ariane Deniset, Pierre Sebban, Rui Prazeres, Jean-Michel Ortega, Bernard van Eerdenbrugh, Lynne Taylor, and Isao Noda.

1. R. Bhargava, I. Levin. Spectrochemical Analysis Using Infrared Multichannel Detectors. Oxford, UK: Blackwell Publishing, 2005.
2. P. Dumas, G.L. Carr, G.P. Williams. "Enhancing the Lateral Resolution in Infrared Microspectroscopy by Using Synchrotron Radiation: Application and Perspectives". Analysis. 2000. 28(1): 68-74.
3. N. Guilhaumou, P. Dumas, G.L. Carr, G.P. Williams. "Synchrotron Infrared Microspectrometry Applied to Petrography in Micrometer-Scale Range: Fluid Chemical Analysis and Mapping". Appl. Spectrosc. 1998. 52(8): 1029-1034.
4. N. Jamin, P. Dumas, J. Montcuit, W.H. Fridmann, G.L. Carr, G.P. Williams. "Chemical Imaging of Living Cells by Synchrotron Infrared Microspectrometry". Proc. of SPIE. 1997. 3153: 133-140.

5. E. Levenson, P. Lerch, M.C. Martin. "Infrared Imaging: Synchrotrons vs. Arrays, Resolution vs. Speed". Infrared Phys. and Techno. 2006. 49: 45-52.
6. S. Amarie, T. Ganz, F. Keilmann. "Mid-Infrared Near-Field Spectroscopy". Opt. Express. 2009. 17(24): 21794-21801.
7. M. Brehm, T. Taubner, R. Hillenbrand, F. Keilman. "Infrared Spectroscopic Mapping of Single Nanoparticles and Viruses at Nanoscale Resolution''. Nano Letters. 2006. 6(7): 1307-1310.
8. A. Cricenti, R. Generosi, P. Perfetti, J.M. Gilligan, H. Tolk, C. Coluzza, G. Margaritondo. ''Free-Electron Laser Near-Field Nanospectroscopy". Appl. Phys. Lett. 1998. 73: 151-154.
9. N. Gross, A. Dazzi, J.-M. Ortega, R. Andouart, R. Prazeres. ''Infrared Near-Field Study of a Localized Absorption in a Thin Film". Eur. Phys. J. Appl. Phys. 2001. 16: 91-98.
10. R. Hillenbrand, T. Taubner, F. Keilmann. "Phonon-Enhanced Light-Matter Interaction at the Nanometer Scale". Nature. 2002. 418(6894): 159-162.
11. M.K. Hong, A.G. Jeung, N.V. Dokholyan, T.I. Smith, H.A. Schwettman, P. Huie, S. Erramilli. "Imaging Single Living Cells with a Scanning Near-Field Infrared Microscope Based on a Free-Electron Laser". Nucl. Instrum. and Methods in Phys. Res., Sect. B. 1998. 144: 246-255.
12. A.J. Huber, D. Kazantsev, F. Keilmann, J. Wittborn, R. Hillenbrand. "Simultaneous IR Material Recognition and Conductivity Mapping by Nanoscale Near-Field Microscopy". Adv. Mater. 2007. 19(17): 2209-2212.
13. F. Huth, M. Schnell, J. Wittborn, N. Ocelic, R. Hillenbrand. "Infrared-Spectroscopic Nanoimaging with a Thermal Source". Nat. Mater. 2011. 10(5): 352-356.
14. B. Knoll, F. Keilmann. "Near-Field Probing of Vibrational Absorption for Chemical Microscopy". Nature. 1999. 399(6732): 134-137. doi:10.1038/20154.
15. F. Keilmann, A.J. Huber, R. Hillenbrand. "Nanoscale Conductivity Contrast by Scattering-Type Near-Field Optical Microscopy in the Visible, Infrared and THz Domains". Journal of Infrared, Millimeter, and Terahertz Waves. 2009. 30(12): 1255-1268. doi: 10.1007/s10762-009-9525-3.
16. D. Palanker, G. Knippels, T.I. Smith, H.A. Schwettman. "IR Microscopy with a Transient Photo-Induced Near-Field Probe". Opt. Commun. 1998. 148: 215-220.
17. A. Piednoir, F. Creuzet, C. Licoppe, J.-M. Ortega. "Locally Resolved Infrared Spectroscopy''. Ultramicroscopy. 1995. 57(2-3): 282-286. doi:10.1016/0304-3991(94)00153.
18. A. Dazzi, S. Goumri-Said, L. Salomon. "Theoretical Study of an Absorbing Sample in Infrared Near-Field Spectromicroscopy". Opt. Commun. 2004. 235: 351-360.
19. A. Dazzi, R. Prazeres, F. Glotin, J.-M. Ortega. "Local Infrared Microspectroscopy with Subwavelength Spatial Resolution with an Atomic Force Microscope Tip Used as a Photothermal Sensor". Opt. Lett. 2005. 30(18): 2388-2390.
20. J. Houel, S. Sauvage, P. Boucaud, A. Dazzi, R. Prazeres, F. Glotin, J.-M. Ortega, A. Miard, A. Lemaître. "Ultraweak-Absorption Microscopy of a Single Semiconductor Quantum Dot in the Midinfrared Range". Phys. Rev. Lett. 2007. 99: 217404. doi: 10.1103/PhysRevLett.99.217404.
21. J. Houel, E. Homeyer, S. Sauvage, P. Boucaud, A. Dazzi, R. Prazeres, J.-M. Ortega. "Midinfrared Absorption Measured at a λ/400 Resolution with an Atomic Force Microscope". Optics Exp. 2009. 17: 10887-10894.
22. S. Sauvage, A. Driss, F. Réveret, P. Boucaud, R. Dazzi, F. Prazeres, J.-M. Glotin, A. Ortéga, Y. Miard, F. Halioua, I. Raineri, A. Sagnes, Lemaître. "Homogeneous Broadening of the S-to-P Transition in InGaAs/GaAs Quantum Dots Measured by Infrared Absorption Imaging with Nanoscale Résolution". Phys. Rev. B. 2011. 83: 035302. doi: 10.1103/PhysRevB.83.035302.
23. C. Policar, J.B. Waern, M.A. Plamont, S. Clède, C. Mayet, R. Prazeres, J.-M. Ortega, A. Vessières, A. Dazzi. "Subcellular IR Imaging of a Metal–Carbonyl Moiety Using Photothermally Induced Resonance''. Angew. Chem. Int. Ed. 2010. 50(4): 860-864.
24. A. Dazzi, R. Prazeres, F. Glotin, J.-M. Ortega, M. Alsawaftah, M. De Frutos. "Chemical Mapping of the Distribution of Viruses into Infected Bacteria with a Photothermal Method". Ultramicroscopy. 2008. 108: 635-641.
25. C. Mayet, A. Dazzi, R. Prazeres, F. Allot, F. Glotin, J.-M. Ortega. "Sub–100-nm IR Spectromicroscopy of Living Cells". Opt. Lett. 2008. 33: 1611-1613.
26. C. Mayet, A. Dazzi, R. Prazeres, J.-M. Ortega, D. Jaillard. "In Situ Identification and Imaging of Bacterial Polymer Nanogranules by Infrared Nanospectroscopy". Analyst. 2010. 135: 2540-2545.
27. K. Kjoller, J.R. Felts, D. Cook, C.B. Prater, W.P. King. "High-Sensitivity Nanometer-Scale Infrared Spectroscopy Using a Contact Mode Microcantilever with an Internal Resonator Paddle". Nanotechnology. 2010. 21(18): 185705. doi:10.1088/0957-4484/21/18/185705.
28. C. Prater, K. Kjoller, D. Cook, R. Shetty, G. Meyers, C. Reinhardt, J. Felts, W. King, K. Vodopyanov, A. Dazzi. "Nanoscale Infrared Spectroscopy of Materials by Atomic Force Microscopy''. Microscopy and Analysis. 2010. 24(3): 5-8.
29. A. Dazzi, R. Prazeres, F. Glotin, J.-M. Ortega. "Subwavelength Infrared Spectromicroscopy Using an AFM as a Local Absorption Sensor". Infrared Phy. Techno. 2006. 49: 113-121.
30. A. Dazzi, R. Prazeres, F. Glotin, J.-M. Ortega. "Analysis of Nano-Chemical Mapping Performed by an AFM-based ("AFMIR") Acousto-Optic Technique". Ultramicroscopy. 2007. 107(12): 1194-1200.
31. G.A. Hill, J.H. Rice, S.R. Meech, D.Q.M. Craig, P. Kuo, K. Vodopyanov, M. Reading. "Submicrometer Infrared Surface Imaging Using a Scanning-Probe Microscope and an Optical Parametric Oscillator Laser". Opt. Lett. 2009. 34: 431-433.
32. C. Marcott, M. Lo, K. Kjoller, C. Prater, I. Noda. "Spatial Differentiation of Sub-Micrometer Domains in a Poly(hydroxyalkanoate) Copolymer Using Instrumentation that Combines Atomic Force Microscopy (AFM) and Infrared (IR) Spectroscopy". Appl. Spectrosc. 2011. 65(10): 1145-1150.
33. R. Kranz, K. Gabbert, T. Locke, M. Madigan. "Polyhydroxyalkanoate Production in Rhodobacter Capsulatus: Genes, Mutants, Expression, and Physiology". Appl. and Environ. Microbiol. 1997. 63(8): 3003-3009.
34. H.H. Wong, S.Y. Lee. "Poly-(3-hydroxybutyrate) Production from Whey by High-Density Cultivation of Recombinant *Escherichia coli*". Appl. Microbiol. Biotechnol. 1998. 50: 30-33.
35. Q. Zhao, G. Cheng. "Preparation of Biodegradable Poly(3-hydroxybutyrate) and Poly(ethylene glycol) Multiblock Copolymers". J. Mat. Sci. 2004. 39: 3829-3831.
36. D. Naumann. "FT-IR and FT-NIR Raman Spectroscopy in Biomedical Research". The Eleventh International Conference on Fourier Transform Spectroscopy, AIP Conference Proceedings. 1998. 430: 96-109.
37. S.K. Hahn, H.W. Ryu, Y.K. Chang. "Comparison and Optimization of Poly(3-hydroxybutyrate) Recovery from Alcaligenes Eutrophus and Recombinant Escherichia Coli". Korean Journal Chem. Eng. 1998. 15(1): 51-55.
38. D. Jendrossek, O. Selchow, M. Hoppert. ''Poly(3-hydroxybutyrate) Granules at the Early Stages of Formation are Localized Close to the Cytoplasmic Membrane in Caryophanon Latum". Appl. and Environ. Microbiol. 2007. 73(2): 586-593.
39. M.M. Satkowski, D.H. Melik, J.-P. Autran, P.R. Green, I. Noda, L.A. Schechtman. "Physical and Processing Properties of Polyhydroxyalkanoate Copolymers". In: Y. Doi, A. Steinbuchel (ed.) Biopolymers, vol. 3B, Weinhiem: Wiley-VCH, 2001. Pp. 231-264.
40. I. Noda, P.R. Green, M.M. Satkowski, L.A. Schechtman. "Preparation and Properties of a Novel Class of Polyhydroxyalkanoate Copolymers''. Biomacromolecules. 2005. 6(2): 580-586.
41. I. Noda, M.M. Satkowski, A.E. Dowrey, C. Marcott. "Polymer Alloys of Nodax Copolymers and Poly(Lactic Acid)". Macromol. Biosci.. 2004. 4(3): 269-275.
42. A. Padermshoke, H. Sato, Y. Katsumoto, S. Ekgasit, I. Noda, Y. Ozaki. ''Thermally Induced Phase Transition of Poly(3-hydroxybutyrate-*co*-3-hydroxyhexanoate) Investigated by Two-Dimensional Infrared Correlation Spectroscopy.'' Vib. Spectrosc. 2004. 36: 241-249.
43. B. Van Eerdenbrugh, M. Lo, K. Kjoller, C. Marcott, L.S. Taylor. ''Nanoscale Mid-Infrared Evaluation of the Miscibility Behavior of Blends of Dextran or Maltodextrin with Poly(vinylpyrrolidone)''. Molec. Pharm. 2012. 9: 1459-1469. doi:10.1021/mp300059z.
44. B. Van Eerdenbrugh, M. Lo, K. Kjoller, C. Marcott, L.S. Taylor. ''Nanoscale Mid-Infrared Imaging of a Drug–Polymer Blend". J. Pharm. Sci. 2012. 101(6): 2066-2073. doi:10.1002/jps.
45. L.A. Utracki. "Glass Transition Temperature in Polymer Blends". Adv. Polym. Technol. 1985. 5: 33-39.
46. A. Newman, D. Engers, S. Bates, I. Ivanisevic, R.C. Kelly, G. Zografi. "Characterization of Amorphous API: Polymer Mixtures Using X-

ray Powder Diffraction". J. Pharm. Sci. 2008. 97: 4840-4856.
47. B. Van Eerdenbrugh, J.A. Baird, L.S. Taylor. "Crystallization Tendency of Active Pharmaceutical Ingredients Following Rapid Solvent Evaporation–Classification and Comparison with Crystallization Tendency from Undercooled Melts". J. Pharm. Sci. 2010. 99: 3826-3838.
48. J.A. Baird, B. Van Eerdenbrugh, L.S. Taylor. "A Classification System to Assess the Crystallization Tendency of Organic Molecules from Undercooled Melts". J. Pharm. Sci. 2010. 99: 3787-3806.
49. Z.M. Huang, Y.Z. Zhang, M. Kotaki, S. Ramakrishna. "A Review on Polymer Nanofibers by Electro-Spinning. Applications in Nanocomposites". Compos. Sci. Technol. 2003. 63: 2223-2253.
50. X. Ma, J. Liu, C. Ni, D.C. Martin, D.B. Chase, J.F. Rabolt. "Molecular Orientation in Electrospun Poly(vinylidene fluoride) Fibers". Macro Lett. 2012. 1: 428-431.
51. A. Dazzi, F. Glotin, R. Carminati. "Theory of Infrared Nanospectroscopy by Photothermal Induced Resonance". J. Appl. Phys. 2010. 107: 124519. doi:10.1063/1.3429214.
52. W. Nowacki. Thermoelasticity, vol. 3. International Series of Monographs on Aeronautics and Astronautics. Oxford, UK: Pergamon Press, Ltd., 1962.
53. D. Sarid. Scanning Force Microscopy. New York: Oxford University Press, 1991.
54. P.A. Yuya, D.C. Hurley, J.A. Turner. "Contact-Resonance Atomic Force for Viscoelasticity". J. Appl. Phys. 2008. 104: 074916–074922.
55. I. Schmitz, M. Schreiner, G. Friedbacher, M. Grasserbauer. "Phase Imaging as an Extension to Tapping Mode AFM for the Identification of Material Properties on Humidity-Sensitive Surfaces". Appl. Surf. Sci. 1997. 115(2): 190-198.
56. L. Landau, E. Lifchitz. Théorie de l'élasticité. Moscow, USSR: MIR, 1967.
57. C.A.J. Putman, B.G. De Grooth, N.F. Van Hulst, J. Greve. "Detailed Analysis of the Optical Beam Deflection Technique for Use in Atomic Force Microscopy." J. App. Phys. 1992. 72(1): 6-12.

APPENDIX: MATHEMATICAL MODEL OF AFM–IR

In this section, we outline the basic theory of the signal detected in AFM–IR. The section below includes a discussion of the following steps:

- Absorption of IR light by the sample
- Generation of heat in the sample and resulting temperature rise
- Thermal expansion pulse of the sample
- Excitation of cantilever resonances from the thermal expansion pulse
- Extraction of cantilever amplitudes at specific resonant modes

The bottom-line of this analysis is that the amplitude of cantilever oscillation at any IR wavelength is directly proportional to the sample absorption coefficient at that wavelength. It is this underlying link that allows the AFM–IR technique to provide IR absorption spectra very well correlated to conventional IR spectroscopy.

Absorption of IR Light by the Sample. Spectroscopy studies interactions of a material with an incident wave as a function of wavelength (or equivalently, energy or frequency). In the mid-IR range (500 to 4000 cm^{-1}), the energy of the electromagnetic waves usually corresponds to molecular vibrations. From an optical point of view, materials are characterized by their complex optical index:

$$\tilde{n}(\lambda) = n(\lambda) + i\kappa(\lambda) \qquad \text{(A1)}$$

where λ is the wavelength, $n(\lambda)$ is the real refractive index, and $\kappa(\lambda)$ the imaginary component of the index is the extinction coefficient. The wavelength dependence of $n(\lambda)$ represents the optical dispersion of a material, while $\kappa(\lambda)$ corresponds to the absorption. We focus on the wavelength dependence of the absorption, which serves as the foundation of IR absorption spectra.

When IR radiation impinges on a sample, the electric field of the electromagnetic wave can be absorbed by a molecule in its path if the radiation frequency matches that of a natural vibrational frequency and induces a dipole moment change in the molecule as a result of the interaction. When molecular vibrations are excited because of absorption of a portion of the incident radiation into a higher vibrational state, heat is produced in the sample matrix when the excited molecules return to their ground vibrational state. The degree of absorption comes from the imaginary part of the dipolar susceptibility of the molecular vibration. The principle of spectroscopy is to measure the intensity of the radiation transmitted through the sample as a function of the wavelength. In the IR spectral range, it is more common to use "wavenumber", (a measure of the radiation frequency) instead the wavelength. If we consider a homogeneous layer of a medium with thickness z and complex optical index $\tilde{n}(\lambda)$, illuminated by an electromagnetic plane wave, the transmitted intensity can be given by the Beer–Lambert Law as (neglecting the index mismatch reflections at the interfaces):

$$I_t = I_{\text{inc}} e^{-4\pi\sigma\kappa z} \qquad \text{(A2)}$$

where I_{inc} is the incident intensity, σ the wavenumber, and κ the extinction coefficient. The transmittance coefficient, T, is defined by the ratio of the transmitted and the incident intensity:

$$T = \frac{I_t}{I_{\text{inc}}} = e^{-4\pi\sigma\kappa z} \qquad \text{(A3)}$$

It is convenient to convert this to an absorbance coefficient, A, which directly gives the variation of the absorption bands as a function of wavenumber:

$$A = \log\frac{1}{T} = \frac{4\pi z}{\ln(10)}\sigma\kappa(\sigma) \qquad \text{(A4)}$$

This simple expression shows that the absorbance is in fact the representation of the extinction coefficient multiplied by the wavenumber. This also means that to make usable spectra with a near-field technique, the microscope will have to measure only the imaginary part of the refractive index.

Generation of Heat from IR Absorption and Resulting Temperature Rise. The absorption of the light by a material leads to an increase in its temperature. The evolution of this heat can be easily described by Fourier's Law:

$$\rho C\frac{\partial T}{\partial t} - k\Delta T = \frac{Q(t)}{V} \qquad \text{(A5)}$$

where ρ is the density, C the heat capacity, k the heat conductivity, V the volume, $Q(t)$ is the absorbed heat, and Δ the Laplace operator. The full mathematical treatment of IR light interacting with an arbitrary shape is complex. In another publication,[51] this subject is treated in more detail. In this review, we provide a simplified approximation that gives the same basic results. If we assume that the intensity of the laser is uniform over the absorbing region of the sample near the atomic force microscope tip and the sample thickness (z) is much smaller than the wavelength, then the power absorbed P_{abs} can be derived from Eq. A2 as:

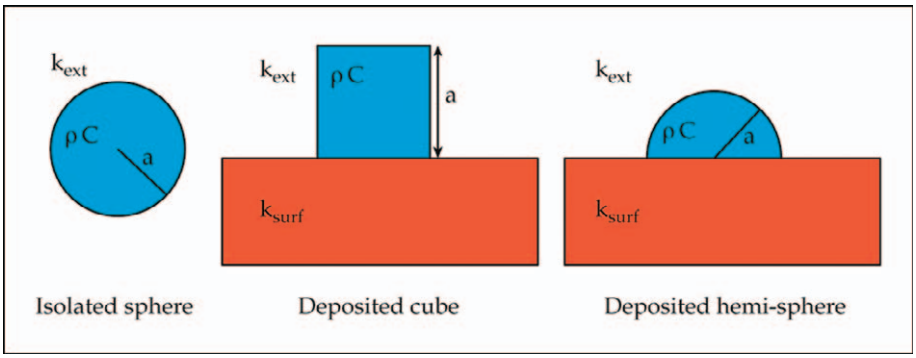

FIG. A1. Schemes of the three different cases of heating: isolated sphere, deposited cube on an infinite surface, and deposited hemi-sphere on an infinite surface.

$$P_{abs} = \int_S (I_{inc} - I_t) dS = 4\pi I_{inc} \sigma\kappa(\sigma) V \tag{A6}$$

where V is the volume of the absorbing object.

For the sake of simplicity, we consider only the case where the pulse duration (t_p) is shorter than the thermal relaxation time of the object. In this case, the heat influx from the IR absorption dominates the heat, leaving the absorber. Moreover, we assume that the heat is absorbed homogeneously inside the object (no temperature gradient). Thus, the increase in temperature during the illumination can be derived from Eq. A5 and becomes:

$$T(t) = \frac{P_{abs}}{V\rho C} t = \frac{4\pi I_{inc}}{\rho C} \sigma\kappa(\sigma) t \tag{A7}$$

where C is the sample heat capacity, ρ is the density, and V is the volume. From Eq. A7, we can define T_{max}, the maximum temperature increase of the sample, as:

$$T_{max} = \frac{P_{abs} t_p}{V\rho C} \tag{A8}$$

When the laser pulse ends, the source of heat disappears and the sample cools. Analytical solutions of the Fourier Eq. A5 are generally possible only for simple geometries, such as a sphere or thin layer. The complete solution for an isolated sphere was treated by Dazzi et al.[51] Even if the temperature behavior cannot be expressed analytically in all cases, it is possible to use finite-element software to find "empirically" the physical law. Comparing solutions for three different cases—isolated sphere, deposited cube on a surface, and deposited hemisphere on a surface (Fig. A1)—we can conclude that the temperature decay at the end of the pulse follows the same law:

$$T(t) = T_{max} \exp\left(\frac{t_p - t}{\tau_{relax}}\right) \tag{A9}$$

where τ_{relax} is the key factor necessary to describe the heat diffusion of the sample. The relaxation time (τ_{relax}) depends strongly on the environment of the sample and on its size:

$$\tau_{relax} = \frac{\rho C}{k_{eff}} a^p \tag{A10}$$

where a is the size of the sample (radius or characteristic length): $k_{eff} = 3k_{ext}$ and $p = 2$ for the case of an isolated sphere, with k_{ext} being the heat conductivity of the surrounding media; $k_{eff} = a_1 k_{ext} + b_1 k_{surf}$ and $p = 1.98$ for the case of deposited cube on a surface, with k_{surf} being the heat conductivity of the surface and k_{ext} the heat conductivity of the surrounding media; and $k_{eff} = a_2 k_{ext} + b_2 k_{surf}$ and $p = 1.989$ for the case of deposited hemisphere on a surface, with k_{surf} the heat conductivity of the surface and k_{ext} the heat conductivity of the surrounding media.

To summarize this section, we can conclude that the behavior of temperature (Fig. A2) when the laser pulse is shorter than the sample time of relaxation because of photothermal absorption can be expressed as:

$$T(t) = T_{max} \frac{t}{t_p} \quad for \quad 0 \le t \le t_p$$

$$T(t) = T_{max} \exp\left(\frac{t - t_p}{\tau_{relax}}\right) \quad for \quad t \ge t_p \tag{A11}$$

With this theoretical approach, it is easy to understand why the estimation of the increase of temperature (or T_{max}) is also a way to measure the absorbance of a sample. All physical phenomena are linear, allowing us to keep the proportionality. The maximum increase in temperature is proportional to the power absorbed by the sample, which is proportional to the absorbance.

Sample Thermal Expansion. When the temperature increases in the body of a material, this leads to the increase in the internal stress, resulting in thermal expansion. The temperature field inside the sample is equivalent to a force field, resulting in deformations that depend on the thermomechanical properties of the sample. An expression that links displacement as a function of the temperature is:[52]

$$(1-2\nu)\nabla^2 \mathbf{u} + \nabla(\nabla \times \mathbf{u}) = 2(1+\nu)\alpha_T \nabla T \tag{A12}$$

where ν is the Poisson coefficient, **u** is the displacement vector, T is temperature, and α_T the thermal expansion coefficient. As for the Fourier Law Eq. A5, the analytical solutions for such an equation are only possible for simple cases with high order of symmetry. With the same idea as the previous section, we studied three different cases (sphere, cube, and hemisphere) by finite element analysis and found that the law of

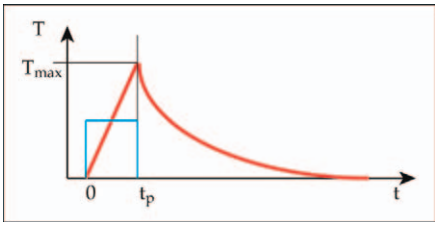

FIG. A2. Evolution of the sample temperature **(red)** *illuminated by a pulsed laser* **(blue).**

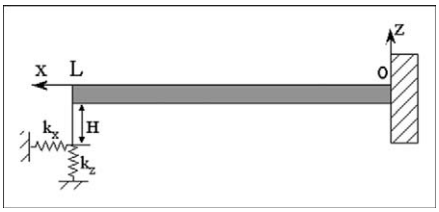

FIG. A3. Atomic force microscope cantilever scheme. The lever is embedded at x = 0, and the length is L. The tip is positioned at x = L − δx. The contact stiffness is represented by two springs, one for the vertical displacement and one for the lateral.

expansion can be written as:

$$\frac{\mathbf{u}(t)}{a} = B\alpha_T T(t) \qquad \text{(A13)}$$

where B is a constant depending on the geometry case (sphere, cube, and hemisphere). The interesting point of Eq. A13 is that it shows the displacement field ($\mathbf{u}$) directly follows the time-dependent temperature (in the case of a non-viscoelastic material).

Excitation of Cantilever Resonances from the Thermal Expansion. The AFM–IR technique measures the thermal expansion resulting from IR absorption by using the tip of an atomic force microscope probe. The rapid thermal expansion creates a force impulse on the tip that results in oscillation of the cantilever at its contact resonance frequencies. To estimate the reaction of the cantilever when the expansion occurs under the tip, we need to go back to the Euler–Bernoulli beam equation:

$$EI\frac{\partial^4 z}{\partial x^4} + \rho S\frac{\partial^2 z}{\partial t^2} + \gamma\frac{\partial z}{\partial t} = W(x,t) \quad \text{(A14)}$$

where E is the cantilever Young modulus, I the area moment of inertia, ρ the density, S the cross section, γ the damping, and W the external mechanical source of motion. The cross section is $S = we$ and the area moment of inertia $I = we^3$ in the case of a rectangular beam, where w and e are the width and thickness, respectively. The x coordinate describes the longitudinal direction, and z represents the deflection of the cantilever (Fig. A3). The tip contact on the sample is modeled by two spring constants, k_x (lateral) and k_z (normal). The cantilever length is L with the clamped extremity at $x = 0$ and the tip positioned at $x = L - \delta x$ (Fig. A4).

The general harmonic solution of the Eq. (A14) is:

$$z(x,t) = g(x)h(t) \qquad \text{(A15)}$$

where

$$\begin{aligned} g(x) = {} & A[\cos(\beta x) + \cosh(\beta x)] \\ & + B[\cos(\beta x) - \cosh(\beta x)] \\ & + C[\sin(\beta x) + \sinh(\beta x)] \\ & + D[\sin(\beta x) - \sinh(\beta x)] \end{aligned}$$

and $h(t) = \exp(i\omega t)$, with β being the wave vector and ω the complex angular frequency.

The boundaries conditions of the cantilever imposed by the clamped end and the tip contact can be cast in the form:

$$\begin{array}{ll} x = 0 & x = L \\ g(x) = 0 & EI\dfrac{\partial^2 g(x)}{\partial x^2} = M \\ \dfrac{\partial g(x)}{\partial x} = 0 & EI\dfrac{\partial^3 g(x)}{\partial x^3} + F_z = 0 \end{array} \qquad \text{(A16)}$$

where M is the bending moment and F_z the reaction force at the lever end. The expression for F_z is found if we consider the deflection $g(L)$ at the end of the lever. The reaction force of the surface is opposite to the displacement at the end of the lever, leading to $F_z = k_z g(L)$, where k_z is the vertical spring constant associated with the linear approximation for a small vibrational amplitude. The bending moment $M = -k_x H^2\left(\frac{\partial g}{\partial x}\right)_{x=L}$ can also be found in relationship to the moment induced by the lateral displacement of the tip by knowing the lateral spring constant k_x and the tip height H (Fig. A4). Substituting the expression for F_z and M into Eq. A16 and using the modal expression of $g(x)$, we obtain the eigenvalue equation of the vibrational modes:[51]

$$\begin{aligned} & -1 + \cos x\cosh x - Vx^3 \\ & (\cos x\sinh x + \sin x\cosh x) \\ & -Ux(\sin x\cosh x - \cos x\sinh X) \\ & -UVx^4(1 + \cos x\cosh x) = 0 \end{aligned} \qquad \text{(A17)}$$

where $U = \frac{k_x L^2}{3k_x H^2}; V = \frac{k_c}{3k_z}; X = \beta L$.

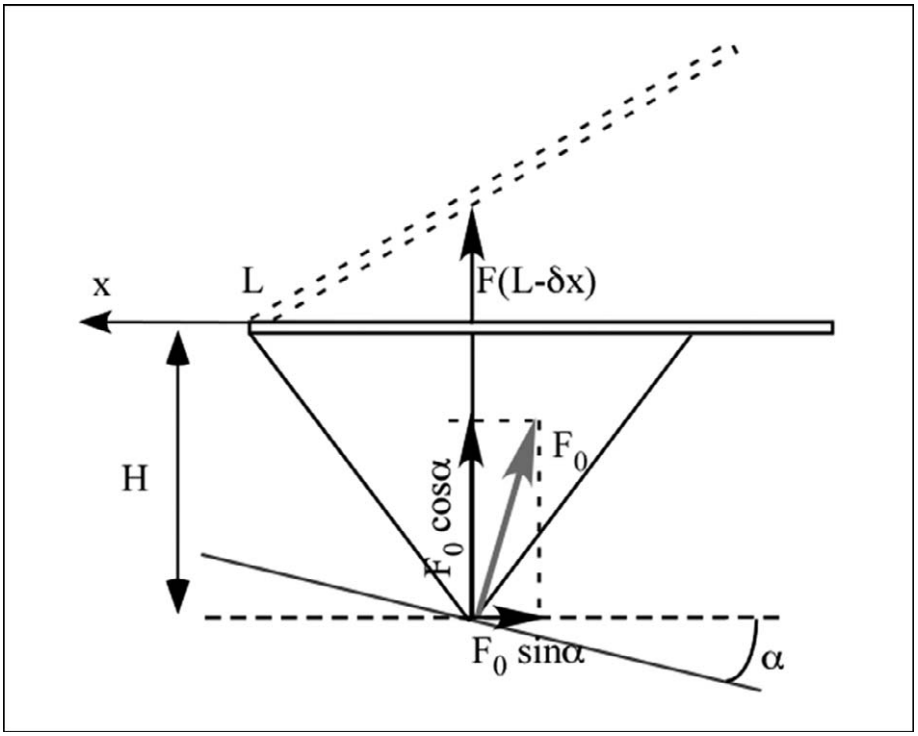

FIG. A4. Scheme of the atomic force microscope tip in contact with the surface. The tilt angle between the cantilever and the surface is α.

This eigenvalue equation is the most general equation for vibration of the cantilever. If the tip is free ($k_x = 0$ and $k_z = 0$), we find the common equation of modes for a free cantilever $1 + \cos x \cosh x = 0$.[53] In the AFM–IR technique, the cantilever tip is kept in contact with the sample by the initial load force. The usual values of the cantilever spring constant k_c employed in contact mode are very small (from 0.03 to 0.2 N/m) compared with the spring constant k_z of the tip-sample contact (around 10^5 N/m), so that the parameter V tends to 0. Moreover, we checked that if we supposed no indentation ($V = 0$), the calculated values of frequencies by the finite element method were in good agreement with those measured experimentally.[30] We denote this specific configuration "contact resonance". This approach is similar to that used by Yuya et al.[54] for contact resonance of visco-elasticity, but in our case, the tip could move laterally and was not allowed to produce indentation into the sample.

As a result, the general eigenvalue equation for the AFM–IR configuration is given by:

$$-1 + \cos x \cosh x - Ux(\sin x \cosh x - \cos x \sinh x) = 0 \quad \text{(A18)}$$

The spatial distribution of mode n in the case of contact resonance is described by:

$$g_n(x) = [\cos(\beta_n x) - \cosh(\beta_n x)] - \left[\frac{\cos(\beta_n L) - \cosh(\beta_n L)}{\sin(\beta_n L) - \sinh(\beta_n L)}\right] [\sin(\beta_n x) - \sinh(\beta_n x)] \quad \text{(A19)}$$

where β_n is the wavevector of the modes solution of the Eigen Eq. A18. One can notice that the value of the mode depends on the value of the lateral stiffness. This property is interesting from a mechanical point of view, because the frequency of the mode will give us the stiffness of the sample.[51] This sort of analysis is equivalent to the phase imaging of the atomic force microscope tapping mode.[55] Combining chemical and mechanical analysis seems a potentially powerful approach for enhancing the ability of the technique to characterize small morphological structures.

In our particular case, the cantilever is excited by a source of motion that is the thermal expansion. The corresponding equation of motion can be written as:

$$EI\frac{\partial^4 z}{\partial x^4} + \rho S\frac{\partial^2 z}{\partial t^2} + \gamma\frac{\partial z}{\partial t} = W(x,t) \quad \text{(A20)}$$

where $W(x,t)$ is the mechanical source of motion, and where the general solution can be expanded as a sum over eigenmodes: $z(x,t) = \sum_n P_n g_n(x) h(t)$, where P_n is the amplitude coefficient of the mode n.

The source term $W(x,t)$ describes the variation of the force induced on the tip by the expansion of the object. We assume that the tip is rigid and transmits this change of force to the cantilever. The tip contact can be characterized by the spring constant k_z, which depends on the impedance of the Young's modulus of the tip and the sample, and the radius of the tip, neglecting the sample curvature compared with the tip.[56] The force received by the tip is given by:

$$F(t) = k_z u(t) = k_z a B \alpha_T T(t) \quad \text{(A21)}$$

The beam modes have a vanishing amplitude at $x = L$ (Eq. A19). In this model, under the expansion of the object, the tip is not able to induce a direct displacement but creates a bending of the lever at $x = L$. Moreover, the angle between the lever and the surface is usually not null (Fig. A4). In order to account for this behavior in the source term, we split the force into two (normal and lateral) components that are applied at a point $x = L - dx$, with $dx << L$. The normal component is $F_{norm}(t) = F(t) \cos(\alpha)$, and the lateral one is $F_{lat}(t) = F(t)\sin(\alpha)\frac{H}{\delta x}$. Therefore, the source term is given by:

$$W(x,t) = \delta(x - L + \delta x)F(t) = K\delta(x - L + \delta x)T(t) \quad \text{(A22)}$$

where $K = [\cos(\alpha) + \frac{H}{\delta x}\sin(\alpha)]Bak_z\alpha_T$. Substituting the expression for the source term (Eq. A22) into equation of motion (Eq. A20) by using Fourier transformation and modal orthogonality properties, we finally find:[54]

$$z(x,t) = \sum_n \frac{J}{\omega_n}\left.\frac{\partial g_n(x)}{\partial x}\right|_{x=L} g_n(x) \left[\sin(\omega_n t)e^{-\frac{\Gamma}{2}t}\right] * T(t) \quad \text{(A23)}$$

where $\omega_n = \sqrt{\frac{EI}{\rho S}}\beta_n^2$, $\Gamma = \frac{\gamma}{\rho S}$, $J = -[\cos(\alpha)\delta x + \sin(\alpha)H]k_z\frac{aB}{\rho S L}\alpha_t$ and * denotes the convolution product.

The signal obtained by the four-quadrant detector, $Q(t)$, is not the complete deformation of the cantilever but only its extremity deflection. It can be expressed as the integrated cantilever slope along the diameter D of the laser diode spot on the cantilever:[57]

$$Q(t) = \sum_n \frac{DJ}{\omega_n}\left[\left.\frac{\partial g_n(x)}{\partial x}\right|_{x=L}\right]^2 \left[\sin(\omega_n t)e^{-\frac{\Gamma}{2}t}\right] * T(t) \quad \text{(A24)}$$

Most of the time, the duration t_p of the laser pulse is short (1 to 20 ns) considering the time response of the cantilever (15 to 40 µs). Applying classical cantilever parameters used to make contact and polymer stiffness imagery to model the sample, the theoretical oscillation of the lever is shown in Fig. A5. We clearly see several oscillations of different periodicity that decrease until 600 µs. This suggests that this analytical approach is sufficient to

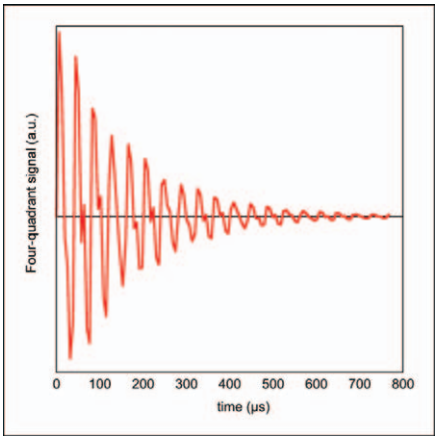

FIG. A5. Temporal response Q(t) of the cantilever excited by a temperature increase generated by pulse laser of 1 ns.

describe the physical phenomenon involved in the technique.

The analysis of the AFM–IR signal is easier to perform in the Fourier domain, revealing the different excitation modes and their amplitudes (Fig. A6). Usually, the analyzed signal is the Fourier transform amplitude, i.e., the modulus of the Fourier transform of $Q(t)$:

$$\begin{aligned}\tilde{Q}(\omega) &= \text{FourierTransf}[Q(t)] \\ &= \sum_n \tilde{Q}_n(\omega) \\ &= \sum_n D|J|\left[\frac{\partial g_n(x)}{\partial x}\right]^2\Bigg|_{x=L} \\ &\quad \frac{|\tilde{T}_{\text{sph}}(\omega)|}{\sqrt{(\omega_n^2-\omega^2)^2+\Gamma^2\omega^2}} \end{aligned} \tag{A25}$$

The Fourier analysis shows that the response of the cantilever is the product of its mode response multiplied by the energy induced by the photothermal effect. In fact, following the expression in Eq. A25, the behavior of each of the modes is the same as a function of temperature. It is typically most convenient to measure the amplitude change in the absorption signal of the fundamental mode, because it possesses most of the energy. The expression of the maximum amplitude of the mode n (at its resonance) is:

$$\tilde{S}_n(\omega_n, \sigma) = H_{\text{m}} H_{\text{AFM}} H_{\text{opt}} H_{\text{th}} \sigma\kappa(\sigma) \tag{A26}$$

where

$$H_{\text{m}} = k_z \alpha_{\text{T}} a B,$$

$$H_{\text{AFM}} = \frac{1}{\Gamma\omega_n}(\cos(\alpha)\delta x + \sin(\alpha)H)\frac{D}{\rho SL}\left(\frac{\partial g_n(x)}{\partial x}\Bigg|_{x=L}\right)^2,$$

$$H_{\text{opt}} = 4\pi I_{\text{inc}},$$

$$H_{\text{th}} = \frac{1}{\rho C} t_p \left(\frac{t_p}{2} + \tau_{\text{relax}}\right)$$

Even if Eq. A26 seems complex, most of the parameters are constant and do not change during an experiment. The final expression of the amplitude of the mode demonstrates the direct proportionality between the absorption of the object (κ) and the signal recorded by the atomic force microscope tip, S_n. As mentioned above, the manner in which an IR spectrum of the sample is obtained is to record the variation of the detector signal S_0 (fundamental mode) as a function of the wavenumber σ. Considering the size of the tip apex in contact with the sample (a few nanometers), we clearly see why there is such interest in a method to make ultra-local spectroscopy measurements.

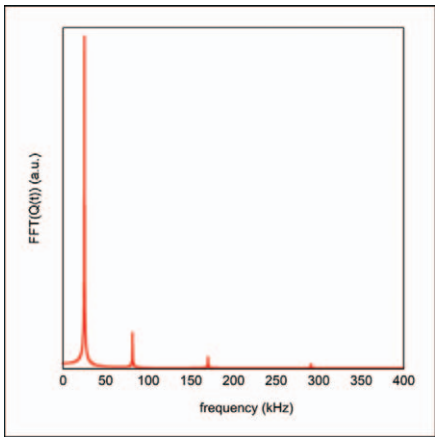

FIG. A6. Fourier transformation representation of the temporal signal Q(t). By this approach, the cantilever modes and their amplitudes are directly obtained.